© 2016. Published by The Company of Biologists Ltd | Development (2016) 143, 703-714 doi:10.1242/dev.129312

RESEARCH ARTICLE

RNA-Seq identifies SPGs as a ventral skeletal patterning cue in sea urchins

Michael L. Piacentino[1,2], Daniel T. Zuch[1,2], Julie Fishman[1], Sviatlana Rose[1], Emily E. Speranza[3], Christy Li[1], Jia Yu[1], Oliver Chung[1], Janani Ramachandran[1], Patrick Ferrell[1], Vijeta Patel[1], Arlene Reyna[1], Hajerah Hameeduddin[1], James Chaves[1], Finnegan B. Hewitt[1], Evan Bardot[1], David Lee[1], Amanda B. Core[1], John D. Hogan[3], Jessica L. Keenan[3], Lingqi Luo[3], Jasmin Coulombe-Huntington[3], Todd A. Blute[1,4], Ekaterina Oleinik[5], Jonas Ibn-Salem[6], Albert J. Poustka[6,7] and Cynthia A. Bradham[1,2,3,*]

ABSTRACT

The sea urchin larval skeleton offers a simple model for formation of developmental patterns. The calcium carbonate skeleton is secreted by primary mesenchyme cells (PMCs) in response to largely unknown patterning cues expressed by the ectoderm. To discover novel ectodermal cues, we performed an unbiased RNA-Seq-based screen and functionally tested candidates; we thereby identified several novel skeletal patterning cues. Among these, we show that SLC26a2/7 is a ventrally expressed sulfate transporter that promotes a ventral accumulation of sulfated proteoglycans, which is required for ventral PMC positioning and skeletal patterning. We show that the effects of SLC perturbation are mimicked by manipulation of either external sulfate levels or proteoglycan sulfation. These results identify novel skeletal patterning genes and demonstrate that ventral proteoglycan sulfation serves as a positional cue for sea urchin skeletal patterning.

KEY WORDS: Patterning, Skeleton, Sulfated proteoglycan, RNA-Seq

INTRODUCTION

Patterning the larval skeleton in sea urchin embryos is a communication-based process in which statically positioned ectodermal cells direct the migration and positioning of primary mesenchymal cells (PMCs), which secrete a calcium carbonate skeleton via biomineralization (Lyons et al., 2012). During gastrulation, the PMCs ingress into the blastocoel, then migrate and organize into a posterior ring around the blastopore, with two ventrolateral clusters from which PMCs migrate anteriorly to form ventrolateral cords. This initial ring-and-cords PMC organization gives rise to the primary skeletal elements, whereas additional migration out of this pattern is required to form the secondary skeletal elements (see Fig. S7A,B for schematics illustrating primary and secondary skeletal patterning).

von Ubisch first suggested that the ectoderm provides patterning instructions to the PMCs in the 1930s (von Ubisch, 1937) and in the early 1960s, Gustafson and Wolpert demonstrated that the posterior PMC ring is actively positioned by posteriorizing the ectoderm and showing that the ring was correspondingly repositioned anteriorly (Gustafson and Wolpert, 1999). In the 1990s, Hardin and colleagues showed that treatment with nickel provokes skeletal patterning defects (Hardin et al., 1992). Armstrong, Hardin and McClay later used microsurgical transplants to demonstrated that the nickel-mediated patterning defect was specific to the ectoderm and not the PMCs (Armstrong et al., 1993). Subsequent experiments have confirmed and corroborated these results (reviewed by Adomako-Ankomah and Ettensohn, 2014; McIntyre et al., 2014). Throughout their migration, the PMCs extend thin filopodia that contact the ectoderm (Gustafson and Wolpert, 1999; Miller et al., 1995). These observations led to the widely accepted hypothesis that the filopodia act as conduits for receiving patterning information from the ectoderm.

Recent studies have identified ectodermal genes whose products regulate PMC migration and skeletogenesis. These include the tripartite motif-containing protein Strim1, the transcription factors Pax2/5/8 and Otp, the signaling ligands FGF, Wnt5a, VEGF and the TGF-β ligand Univin. These genes are expressed in the ectoderm directly adjacent to sites of active biomineralization and with the exception of Univin, which is specifically required for patterning of the secondary skeletal elements (Piacentino et al., 2015), their loss of function (LOF) blocks skeletogenesis, indicating a role in regulating biomineralization (Di Bernardo et al., 1999; Cavalieri et al., 2003; Duloquin et al., 2007; Rottinger et al., 2008; Cavalieri et al., 2011; Adomako-Ankomah and Ettensohn, 2013). Gene products that specifically regulate primary PMC positioning but not biomineralization, i.e. dedicated skeletal patterning genes, remain largely undiscovered.

In contrast to ectodermal skeletal patterning cues, ectodermal specification is better understood. Specification of the ventral ectoderm relies on the asymmetric activation of Nodal expression and signaling, which, in turn, depends on asymmetric p38 activation (Duboc et al., 2004; Flowers et al., 2004; Bradham and McClay, 2006). Nodal induces the ventral expression of BMP2/4, which signals only outside the ventral region to induce dorsal ectodermal specification (Angerer et al., 2000; Duboc et al., 2004). A neurogenic ciliated band develops at the dorsal-ventral (DV) boundary; this default ectodermal state is suppressed by Nodal and BMP2/4 signaling (Duboc et al., 2004; Bradham et al., 2009; Lapraz et al., 2009; Yaguchi et al., 2010). Gene regulatory network models describing ectodermal specification are now established (Su et al., 2009; Saudemont et al., 2010; Barsi et al., 2015), as are initial

[1]Department of Biology, Boston University, Boston, MA 02215, USA. [2]Program in Molecular Biology, Cell Biology and Biochemistry, Boston University, Boston, MA 02215, USA. [3]Program in Bioinformatics, Boston University, Boston, MA 02215, USA. [4]Proteomics and Imaging Core Facility, Boston University, Boston, MA 02215, USA. [5]Scientific Computing and Visualization Group, Boston University, Boston, MA 02215 USA. [6]Max-Planck Institute for Molecular Genetics, Evolution and Development Group, Ihnestrasse 73, Berlin 14195, Germany. [7]Dahlem Center for Genome Research and Medical Systems Biology, Environmental and Phylogenomics Group, Fabeckstraße 60-62, Berlin 14195, Germany.

*Author for correspondence (cbradham@bu.edu)

Received 1 August 2015; Accepted 5 January 2016

Development (2016) 143, 703-714 doi:10.1242/dev.129312

mathematical models describing movement of BMP2/4 in sea urchin embryos (van Heijster et al., 2014).

In this study, we present results from an RNA-Seq-based screen with which we identify novel skeletal patterning genes. LOF analyses indicate that each tested gene is required for normal PMC positioning and skeletal patterning, but not for biomineralization. One such candidate, SLC26a2/7, is a sulfate transporter that is required for a ventral accumulation of sulfated proteoglycans (SPGs) in *Lytechinus variegatus*. Our results demonstrate that ventral SPGs are required to attract PMCs into the ventral portion of the PMC ring, and thereby, to pattern the ventral skeletal rods.

RESULTS

p38 MAPK inhibition in the ectoderm elicits skeletal patterning defects

The goal of this study was to identify novel skeletal patterning genes in the ectoderm of the sea urchin embryo. This project was initiated by the observation that *L. variegatus* embryos cultured in the presence of SB203580 prior to gastrulation develop a strongly mispatterned skeleton (Fig. 1A) (Bradham and McClay, 2006). SB203580 (SB) is a highly specific inhibitor of p38 MAPK (Davies et al., 2000). To test whether SB acts on the ectoderm or the PMCs, we microsurgically generated chimeric embryos in which either the PMCs or the ectodermal hull only were exposed to SB (Fig. 1B). This approach was previously used to show ectoderm-specific skeletal patterning defects with $NiCl_2$ (Armstrong et al., 1993) and overexpression of the homeobox protein Msx (Tan et al., 1998). Patterning defects were observed only in chimeras in which the hull was exposed to SB (Fig. 1C,D), indicating that SB specifically impacts the ectoderm and not the PMCs to induce skeletal patterning defects. PMC migration was disorganized in SB-treated embryos compared with controls (Fig. 1E,F), consistent with defects in the ectodermal cues that mediate PMC positioning. Interestingly, the PMCs in SB-treated embryos progressively displayed excessively numerous and elongated filopodia during gastrulation, which were most conspicuous at late gastrula (LG) stage (Fig. 1F). Filopodia extended by the PMCs are likely to be conduits of information between the ectoderm and the PMCs (Miller et al., 1995; Lyons et al., 2012); the abnormal filopodia observed in SB-treated embryos probably reflect a response to abnormal ectodermal patterning information.

Interestingly, the defect in skeletal patterning, its ectodermal dependence and the abnormal filopodia induced by SB treatment are each similar to the effects of $NiCl_2$ (Hardin et al., 1992; Armstrong et al., 1993; Miller et al., 1995). Thus, both nickel- and SB-treated embryos exhibit characteristics consistent with abnormal ectodermal patterning information, including the spatial disordering of the PMCs, their excessive filopodial extensions and the abnormal skeletons eventually produced. These results suggested the hypothesis that at least some skeletal patterning genes are similarly perturbed in the ectoderm of both nickel- and SB-treated embryos. We reasoned that the simplest explanation for these observations is a loss of ectodermal patterning gene expression with nickel or SB, since PMCs appear to lack a complete set of migration cues (Fig. 1E,F); however, we recognized that it is also possible that increased and/or ectopically expressed cues are responsible for these patterning defects.

SB and nickel have opposite effects on ectodermal specification and differentiation

Treatment with nickel provokes ectodermal ventralization, whereas SB treatment blocks it (Hardin et al., 1992; Bradham and McClay, 2006). We confirmed these effects by comparing the expression of dorsal and ventral specification markers, and by labeling the ciliary band, which is sensitive to DV perturbations (Yaguchi et al., 2010). Nickel exposure resulted in radial expansion of the ventral marker *nodal*, loss of the dorsal marker *tbx2/3* and abnormal restriction of the ciliary band to the posterior region of the embryo (Fig. 1Gb,Hb, Ib), consistent with ventralization. By contrast, SB exposure provoked the opposite effects, with a loss of *nodal* expression, radial expansion of *tbx2/3* and loss of restriction of the ciliary band (Fig. 1Gc,Hc,Ic), consistent with a pre-ventralized ectodermal state (Duboc et al., 2004; Bradham and McClay, 2006). These results indicate that nickel and SB have distinct effects on DV specification and differentiation in the ectoderm. This conclusion led us to predict that nickel and SB treatments would provoke reciprocal effects on the expression of genes involved in DV specification ('DV genes') in the ectoderm, thereby providing a means to discriminate reciprocally regulated ectodermal DV genes from mutually regulated skeletal patterning genes.

A differential RNA-Seq screen identifies novel skeletal patterning genes

The combined observations that Ni and SB each provoke similar effects on skeletal patterning and opposite effects on ectodermal DV specification provided an opportunity to identify a subset of ectodermal skeletal patterning genes, which we predicted would be regulated similarly by nickel and SB compared with controls and therefore distinguishable from DV genes, which we predicted would be reciprocally regulated by nickel and SB (Fig. 2A). Although the mutually regulated subset of genes might not represent all skeletal patterning genes, and in fact would exclude any patterning genes regulated by the DV gene regulatory network, we reasoned that this approach was still likely to identify novel patterning genes. We further predicted that most non-ectodermal genes would be unaffected by either treatment (Fig. 2A). Finally, we predicted that ectodermal skeletal patterning genes would encode proteins that are associated with the cell surface or secreted, as mediators of communication between the ectoderm and the PMCs.

Following this rationale, we used RNA-Seq to compare the transcriptomes from control, nickel- and SB-treated embryos at the LG stage, and focused on genes downregulated by nickel and SB. An early transcriptome assembly using SOAPdenovo was used to identify candidates downregulated by both nickel and SB ('mutually downregulated', cut-off ≥twofold), which corresponded to a minority subset of the total transcriptome (Fig. S1A), and which, for the identifiable subset, exhibited an approximately twofold enrichment of sequences encoding cell surface or secreted proteins (Fig. S1B). Multiple candidates for further analysis were selected based on this early assembly, along with one candidate that was upregulated by both treatments in the initial assembly (Fig. S1C; Table S1; see supplementary Materials and Methods for the rationale for candidate selection). Subsequently, an improved, final assembly was generated using the SOAPdenovo-Trans (Fig. 2B-F). The fraction of mutually downregulated sequences increased in the final assembly, reflecting substantially improved gene models and annotations, whereas enrichment of cell surface and secreted sequences was maintained (Fig. 2C,D). The directionality of the expression level differences for the selected candidates was maintained in the final assembly, although in some cases, the magnitude of change was reduced such that most candidates from the initial assembly were retained in the final assembly with a cut-off of 1.5-fold (Fig. 2E,F). The candidate genes identified in the final assembly are listed in Table S2. Genes previously implicated in regulating skeletal

Development (2016) 143, 703-714 doi:10.1242/dev.129312

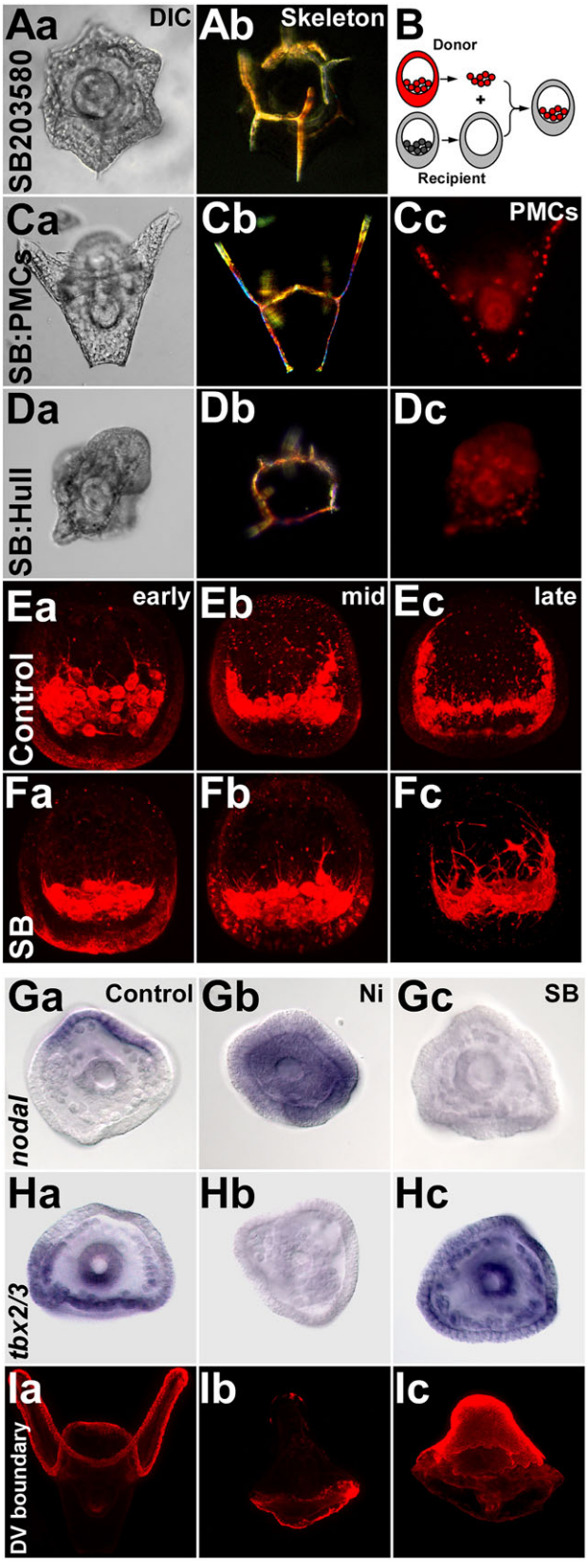

Fig. 1. Ectodermal p38 MAPK inhibition results in skeletal patterning defects and blocks ventral ectodermal specification. (A) Morphology (Aa) and skeletal birefringence (Ab) of a sea urchin embryo treated with SB203580 (SB) prior to gastrulation. (B) Schematic depicting PMC transplants, with Rhodamine-labeled donor PMCs transplanted into unlabeled recipient ectodermal hulls at mesenchyme blastula stage. (C,D) Morphology (Ca,Da), skeletal pattern (Cb,Db) and PMC positioning (Cc,Dc) is shown for chimeras in which only the donor PMCs (C) or the recipient hull (D) was exposed to SB. (E,F) PMC-specific immunostaining shown in control (E) and SB (F) embryos at early (Ea,Fa), mid (Eb,Fb) and late gastrula (Ec,Fc) stages (14, 16 and 18 hpf, respectively). (G,H) Whole-mount *in situ* hybridization for ventrally expressed *nodal* (G) and dorsally expressed *tbx2/3* (H) in control (Ga, Ha), Ni (Gb,Hb) and SB (Gc,Hc) embryos at late gastrula stage. (I) The dorsal-ventral ectoderm boundary is shown by ciliary band-specific immunostaining in control (Ia), Ni (Ib) and SB (Ic) pluteus stage larvae (48 hpf).

patterning exhibited reciprocal rather than mutual regulation by nickel and SB (Fig. 2E,F), indicating first that the identified genes are regulated distinctly from previously described patterning genes, and second, that the candidate pool does not represent a comprehensive set of patterning genes. iPAGE analysis (Goodarzi et al., 2009) shows that GO terms associated with cell surface or extracellular processes (i.e. GPCRs, scavenger receptors and transporters) are enriched in the mutually downregulated set of transcripts (Fig. 2G). We also observed enrichment of GO terms associated with fatty acid biosynthesis and sulfotransferase activity.

To gain a more comprehensive view of the impact of nickel and SB on gene expression, we examined the expression of previously characterized genes (Fig. S1D-H). As expected, most genes involved in ventral ectodermal specification were upregulated by nickel and downregulated by SB (Fig. S1D). Genes involved in dorsal ectodermal specification were downregulated by nickel, and not strongly impacted by SB (Fig. S1E). Most endomesodermal specification genes were not strongly affected by nickel or SB (Fig. S1F-H), with the exception of known dorsal and ventral secondary mesenchyme cell (SMC) genes, which responded reciprocally to nickel and SB, and coelomic and germline genes, which were downregulated by SB. Among this set of 81 genes, only one, SM30, exhibited downregulation by both nickel and SB. SM30 is a biomineralization gene whose protein products are incorporated into the skeleton. Surprisingly, SM30 was recently shown to be dispensable for normal skeletogenesis (Wilt et al., 2013). Thus, most of the known specification and differentiation genes responded as expected to nickel and SB treatments. To investigate the behavior of the metabolic network in nickel- and SB-treated embryos, we performed an iPath 2.0 analysis (Yamada et al., 2011), which indicates that very few metabolic genes were affected by either treatment (Fig. S1I,J). Together, these results are consistent with the predictions schematized in Fig. 2A.

We selected nine candidate genes for functional analysis based on their ‘double-down’ expression profiles. One final candidate gene was selected based on its ‘double-up’ behavior. Morpholino (MO)-mediated knockdown of all ten genes resulted in skeletal patterning but not biomineralization defects, suggesting that the extracellular fraction of the mutually regulated genes is enriched for skeletal patterning cues. We focused on four of these genes for further analyses and obtained their full-length clones (Fig. S1C). Phylogenetic analyses confirmed the annotations for these candidate genes (Fig. S2B-G). To perform functional analyses, we designed translation- or splice-blocking MO antisense oligonucleotides (Fig. S2A). In all four cases, LOF resulted in plutei that displayed dramatic, previously unreported skeletal patterning defects (Fig. 2H,I), indicating that each candidate is required for normal skeletal patterning. The defective skeletal patterns presented reflect commonly observed phenotypes for each of the indicated MOs based on extensive skeletal scoring and include ventral defects induced by SLC MO, right side defects

Development (2016) 143, 703-714 doi:10.1242/dev.129312

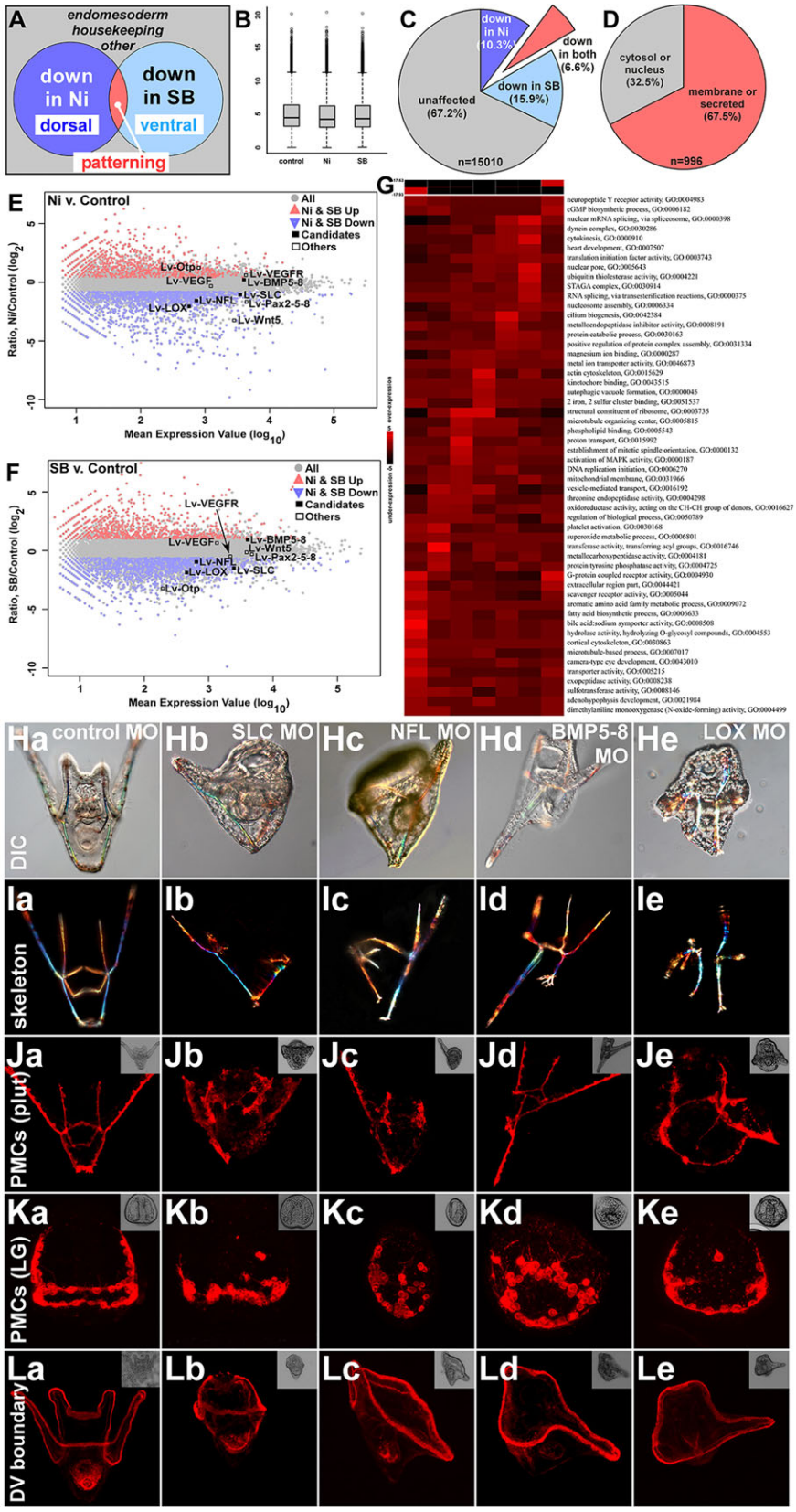

Fig. 2. A differential RNA-Seq-based screen identifies skeletal patterning genes in the sea urchin embryo. (A) Schematic representation of the rationale for the screen. (B) Box plots depicting the range of expression values following normalization of RNA-Seq data. (C,D) Pie charts display differential analysis results from the final RNA-Seq assembly. From the mutually downregulated set of scaffolds (C, red), the intra- and extracellular localization of the identifiable subset is shown (D). (E,F) Differential expression values are shown in MA plots for Ni (E) and SB (F) compared with control. Mutually upregulated (red) and downregulated (blue) scaffolds are shown. Validated skeletal patterning candidates and other genes implicated in skeletal patterning are indicated. (G) iPAGE analysis showing enrichment of GO terms as a heat map with bins reflecting the range of ratios of the average gene expression in Ni and SB embryos compared with control expression. Mutually downregulated bins are to the left and mutually upregulated bins are to the right. (H-L) Loss-of-function analysis for four skeletal patterning candidate genes is shown as morphology (DIC; H), skeletal pattern (I), PMC immunostaining at late gastrula stage (18 hpf; K) and PMC (J) and ciliary band (L) immunostaining at pluteus stage (48 hpf), for embryos injected with the indicated MO. Corresponding phase-contrast images are displayed as insets. The pluteus stage PMC stain and ciliary band control embryos (Ja,La) were uninjected.

induced by NFL MO, left side defects induced by BMP5-8 MO, and midline defects induced by LOX MO (see Fig. S7A-C for scoring rubric). Detailed analyses for LOX, NFL and BMP5-8 will be presented in follow-up studies. Notably, while both Ni and SB treatments provoked radialized skeletons that reflect DV perturbations, none of the candidate LOF phenotypes were radialized. In addition, none of the morphants exhibit a block to biomineralization, since all the PMCs within these larvae were

Development (2016) 143, 703-714 doi:10.1242/dev.129312

associated with skeletal elements (Fig. 2J). Thus, the candidate LOF effects are distinct from those produced by knockdown of VEGF/R, Wnt5a, Otp, Pax2/5/8 or FGF, because each of the latter LOFs blocks biomineralization, resulting in larvae that lack skeletons entirely (Di Bernardo et al., 1999; Cavalieri et al., 2003; Duloquin et al., 2007; Rottinger et al., 2008; Cavalieri et al., 2011; Adomako-Ankomah and Ettensohn, 2013; McIntyre et al., 2013). Furthermore, each candidate LOF resulted in perturbed PMC organization at the LG stage (Fig. 2K), indicating that each gene is required for normal PMC positioning. Finally, we tested ectodermal DV specification by labeling the ciliary band in the LOF embryos. The results show that the ciliary band is restricted normally in each morphant (Fig. 2L), indicating that DV specification of the ectoderm is normal in candidate gene morphants. These results show that the skeletal patterning defects observed in candidate gene morphants do not result from DV perturbations, consistent with their non-radialized phenotypes. These MOs were variably penetrant, ranging from 58 to 88% of the injected embryos (Fig. S3A). The specificity of these MOs is demonstrated by phenotypic rescues when exogenous, nonbinding cognate mRNA *LvNfl*, *LvBmp5-8* and *LvLox* was coinjected (Fig. S3B-D); SLC rescue experiments are presented in Fig. 3T-X. RT-PCR analysis indicates that the splice-blocking SLC MO, NFL MO and BMP5-8 MO each disrupt normal splicing (Fig. S3E-G). SLC MO and BMP5-8 MO each efficiently blocked the formation of the targeted splice junction; sequencing of the mis-spliced bands confirms that SLC MO inhibits inclusion of exon 14 as expected, whereas BMP5-8 MO inhibits the inclusion of exons 2 and 3. NFL MO was less efficient at inhibiting splicing; sequence analysis of the mis-spliced band indicates that only 46 bp at the 3′ end of the targeted exon were excluded; this loss resulted in a frameshift of the downstream sequence. Together, these results demonstrate that the RNA-Seq screen successfully identified novel genes that are required for normal skeletal patterning and PMC positioning, but not for ectodermal DV specification.

LvSlc26a2/7 encodes a sulfate transporter that is required for production of sulfated proteoglycans

Of the four candidates highlighted herein, SLC LOF produced the most dramatic effects, including losses of primary skeletal elements (Fig. 2Hb,Ib). SLC was therefore selected for more extensive analysis. SLC was annotated as a member of the SLC26 family of transmembrane ion transporters. Phylogenetic analyses and sequence alignments place this gene between the vertebrate *SLC26A2* and *SLC26A7* genes (Fig. S2B and Fig. S3B); we will therefore refer to this gene as *LvSlc26a2/7* (SLC). Domain analysis shows that SLC encodes a 10-pass transmembrane protein with domains characteristic of sulfate transporter genes (Fig. S4A). At LG stage, SLC is expressed in the ventral ectoderm, extending from the posterior to the anterior pole, as well as in the blastopore and endoderm (Fig. 3A). SLC expression is maintained throughout early development and is downregulated following gastrulation (Fig. 3B); this expression profile agrees with that of its *S. purpuratus* ortholog, which is annotated as SpPrestin (Tu et al., 2014). Thus, SLC is expressed at the correct time and place to contribute to PMC positioning and skeletal patterning. SLC expression is downregulated in nickel- and SB-treated embryos, corroborating our RNA-Seq results (Fig. 3C and Fig. S5).

The vertebrate *SLC26A2* ortholog encodes a sulfate transporter that is required for the sulfation of proteoglycans (PGs) (Mount and Romero, 2004). Mutation of *SLC26A2* causes the human disorder diastrophic dysplasia, hallmarked by a range of cartilage defects and dwarfism; similar effects occur in SLC26A2-knockout mice, along with skeletal patterning defects. These defects result from reduced sulfation of PGs during chondrogenesis, which, in turn, reduces FGF and Ihh signaling, interfering with skeletal growth (Rossi et al., 1998; Mount and Romero, 2004; Forlino et al., 2005; Gualeni et al., 2010). These findings suggested that LvSLC is also a sulfate transporter responsible for the sulfation of PGs. We tested this by performing Alcian Blue staining using conditions specific for detection of sulfated proteoglycan (SPG). In control embryos, Alcian Blue staining is strongest in the ventral ectoderm, extending from the posterior to the anterior pole and in the blastopore (Fig. 3D, Fig. S6). The ventral accumulation of SPGs closely matches the spatial expression of LvSLC (compare Fig. 3A and D). By contrast, SLC MO-injected embryos exhibited uniformly low SPG levels (Fig. 3G), indicating that SLC is required for the ventral SPG accumulation. To corroborate these results, we tested the effects of culturing embryos in sulfur-free or chlorate-supplemented sea water. We reasoned that removing external sulfate should phenocopy loss of a sulfate transporter; chlorate inhibits the addition of sulfate to the universal sulfate donor PAPS, thereby blocking proteoglycan sulfation (Baeuerle and Huttner, 1986). Previous work showed that sulfated proteoglycans regulate DV specification in sea urchin embryos (Bergeron et al., 2011) and consistent with those results, we found that removal of sulfur or addition of chlorate to early embryos perturbed the DV axis (not shown). To avoid this, we began each treatment at 10 h post fertilization (hpf), after the DV axis is established, but before PMC ingression and migration (Bradham and McClay, 2006; Piacentino et al., 2015). Both treatments provoked uniformly low SPG levels, similar to results with SLC MO (Fig. 3E,F). We corroborated the spatial distribution of SPGs in controls and in no-sulfur embryos by staining with Cuprolinic acid, which selectively labels SPGs (Fig. S6) (Chan et al., 1992). When we overexpressed SLC, the embryos displayed uniformly high SPG levels in the ectoderm (Fig. 3H); this effect was mimicked by culturing embryos in sea water containing increased sulfate concentrations (Fig. 3I). Because of embryo-to-embryo variability, we could not quantitate the Alcian Blue signal across populations; instead, we calculated the ventral-to-dorsal signal difference within individuals, then averaged that ratio (Fig. 3J). The results show that control embryos reproducibly exhibited higher ventral SPG levels, whereas all the treated embryos showed significantly reduced DV ratios. These results demonstrate that SLC is required to establish ventral SPG accumulation.

Ventral SPGs are required for ventral skeletal development

We next examined larval skeletal patterning with our suite of perturbations. Because specific skeletal patterning defects varied from pluteus to pluteus, we comprehensively scored skeletal patterns in each perturbant, including the presence and absence of each rod, defects in rod orientation, and rod transformations or duplications (Fig. S7A-C). No-sulfur, chlorate and SLC MO each resulted in frequent bilateral loss of the primary skeletal elements known as the ventral transverse rods (VTs) (Fig. 3L-N,Q; red arrows and red elements in schematics). Although other skeletal elements were also perturbed by the suite of SPG perturbations, the VTs were most specifically perturbed among the primary skeletal elements, and were the only element for which the impact of all the SLC/SPG perturbations correlated (Fig. S7D). The absence of the VTs correlated strongly with the occurrence of

Development (2016) 143, 703-714 doi:10.1242/dev.129312

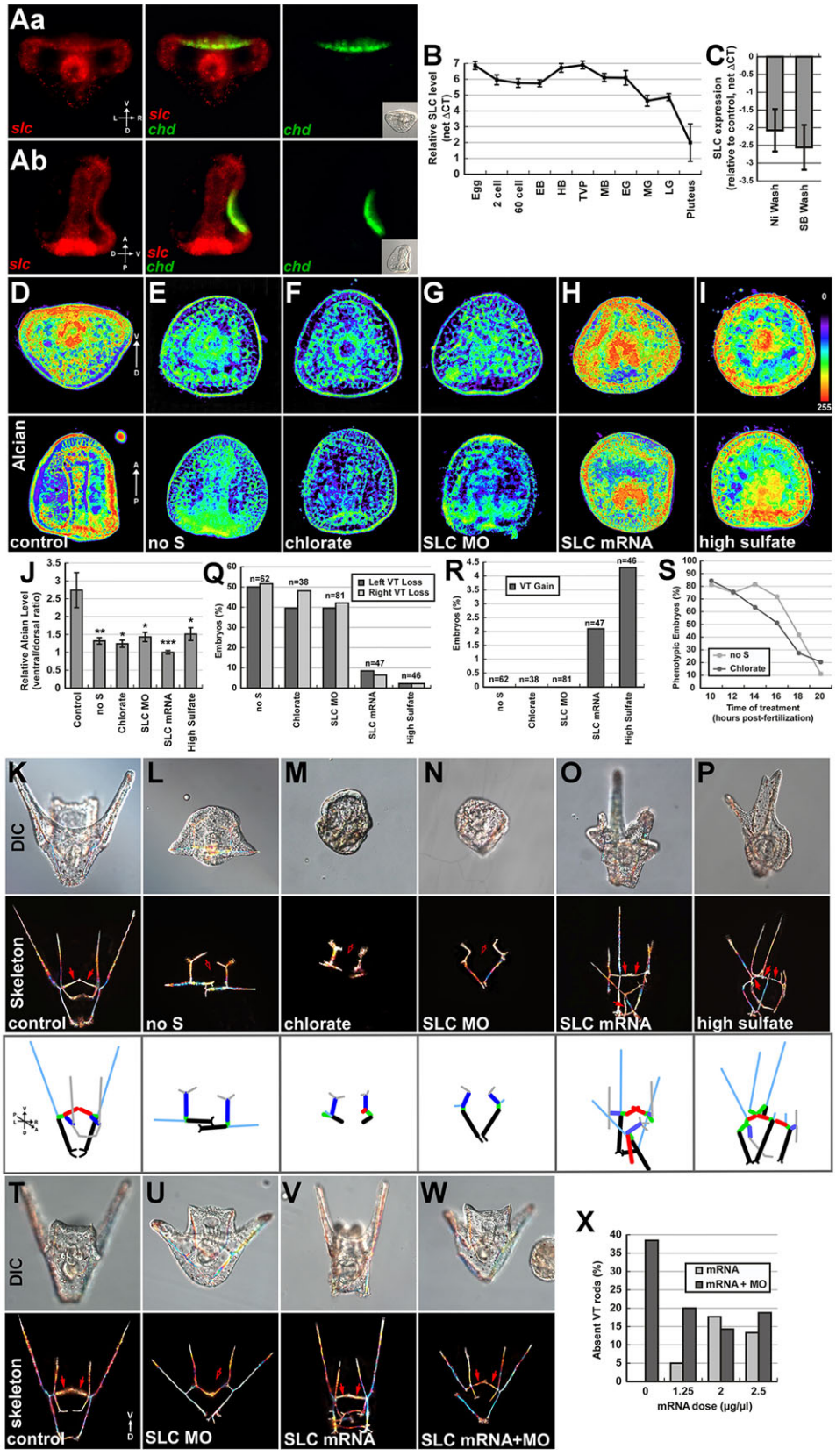

Fig. 3. *slc26a2/7*-dependent ventral sulfated proteoglycans are required for the formation of the ventral transverse skeletal elements. (A) Spatial expression of *slc26a2/7* (red, *slc*) and ventral marker *chordin* (green, *chd*) is shown at late gastrula stage in posterior (Aa) and lateral (Ab) views. Corresponding DIC images are shown as insets. (B) Relative temporal expression of *slc26a2/7* is displayed as normalized ΔC_T values at 11 developmental timepoints ranging from egg to pluteus stages, as means ±s.e.m. (C) *slc26a2/7* expression levels in Ni and SB embryos compared with controls at late gastrula stage are shown as means±s.e.m. (D-I) Alcian Blue staining of sulfated proteoglycans at late gastrula stage with the indicated treatments, shown in posterior (top panels) and lateral (bottom panels) views. Images were pseudocolored using the indicated key to highlight differences in staining intensity. (J) Relative Alcian Blue staining is displayed as the ratio of ventral-dorsal staining intensity in control and perturbed embryos, and is shown as mean±s.e.m.; two-tailed Student's *t*-test **P*<0.05, ***P*<0.005, ****P*<0.0005 compared with control; $n \geq 10$ for all conditions. (K-P) Pluteus stage (48 hpf) morphologies and skeletal patterns are shown for the indicated treatments. The bottom panel shows skeletal schematics, with the ventral transverse (VT) elements indicated in red. Filled or open red arrows indicate VT presence or absence, respectively. (Q,R) Quantitation of the frequency of VT loss (Q) and gain (R) with the indicated treatments. (S) Quantitation of the fraction of phenotypic embryos resulting from treatment time courses with no sulfur or chlorate. (T-W) Morphology and skeletal patterns for embryos injected with SLC MO (U), mRNA (V) or combination (W). Filled or open red arrows indicate VT presence or absence, respectively. (X) Quantitation of VT loss in the SLC rescue experiments. The SLC MO dose was held at 1.33 mM and mRNA dose was varied as indicated.

'midline defects', referring to skeletons with no central elements (Fig. S7E). The VTs initially arise along the posterior ventral ectoderm at the LG stage, coinciding with the location of high SPG levels in controls (see Fig. 3D and Fig. S7A-C). These results indicate that SLC and SPGs are required for VT development. High-sulfate treatment and SLC mRNA injections provoked the development of extra VTs, albeit at a low frequency (Fig. 3O,P,R). Although SLC mRNA and high sulfate provoked

Development (2016) 143, 703-714 doi:10.1242/dev.129312

VT gains less frequently than VT losses (Fig. 3Q-R), VT gains were never observed in SLC/SPG LOF embryos, and so their occurrence with the SLC/SPG gain-of-function (GOF) embryos is noteworthy. SLC/SPG GOF also resulted in the duplication and transformation of other skeletal elements (Fig. S7E). The formation of other skeletal elements was also inhibited by SLC/SPG LOF and GOF (Fig. S7D); however, these defects did not correlate across the treatments and occurred in secondary skeletal elements, suggesting that the principal defect in SLC/SPG perturbants is the loss of the primary VT skeletal elements. To define the developmental time interval during which SPGs are required for skeletal patterning, we performed treatment time courses with no sulfur or with chlorate. Treatments at 10 hpf resulted in the highest frequency of skeletal patterning defects and the penetrance of this effect decreased during gastrulation (Fig. 3S). Treatment at 16 hpf resulted in VT defects (not shown), indicating that their patterning occurs during gastrulation. These results show that ventral SPGs are required during gastrulation for the formation of the VTs. Rescue experiments were performed by co-injection of SLC MO and SLC mRNA, and show that exogenous SLC mRNA rescues VT formation in morphants (Fig. 3T-X), indicating that re-addition of SLC mRNA effectively restores the most consistent patterning defect, and that SLC MO-mediated loss of VTs is not an off-target effect.

Ventral SPGs are necessary and sufficient to attract PMCs ventrally

We next examined PMC positioning at the LG stage with our suite of perturbations. As with the skeletal patterning defects, we observed variable PMC positioning defects. We therefore established a PMC scoring approach, for which we extracted PMC coordinates from confocal image stacks, then modeled the 3D position of each PMC. Tbx2/3 is dorsally expressed in all three germ layers, and thus is expressed in dorsal, but not ventral, PMCs (Croce et al., 2003; Gross et al., 2003). We used ectodermal Tbx2/3 expression as a dorsal landmark to orient each 3D model, and examined each confocal slice in the stack to score each PMC for Tbx2/3 expression.

SLC MO injection resulted in a significant reduction in the fraction of ventrally positioned PMCs (Fig. 4Ce, red; E). Treatment with no sulfur or chlorate similarly provoked a significant reduction in ventral PMC positioning (Fig. 4Cc,d,E). This agrees with previous studies on sulfate-deprived embryos, which exhibited defective PMC migration (Katow and Solursh, 1981). Conversely, SLC mRNA provoked a significant increase in the fraction of ventrally positioned PMCs, as did sulfate-supplemented sea water (Fig. 4Cf,g,E). These results correlate well with the skeletal patterning defects, since the PMCs in the ventral ring produce the VTs (see Fig. S7A-C). As SPG loss (no sulfur, chlorate, or SLC MO) blocks ventral PMC localization and VT formation, whereas SPG gain (SLC mRNA or high sulfate) promotes excessive ventral PMC localization and VT formation, we conclude that ventral SPGs provide an attractive cue that is necessary and sufficient for ventral PMC localization and VT formation. Thus, SLC is a primary ventral skeletal patterning gene.

During this analysis, we also observed an unexpected change in Tbx2/3 expression within the PMCs. In control and control MO-injected embryos, almost none of the dorsal PMCs were Tbx2/3-negative, whereas surprisingly, SPG loss and gain each provoked a striking and significant increase in the percentage of Tbx2/3-negative PMCs in the dorsal ring (Fig. 4D,F). These results indicate that the normal concentration of ventral SPGs is required for robust induction of Tbx2/3 expression in the dorsal PMCs, whereas deviations above or below that level reduce Tbx2/3 expression in the dorsal PMCs.

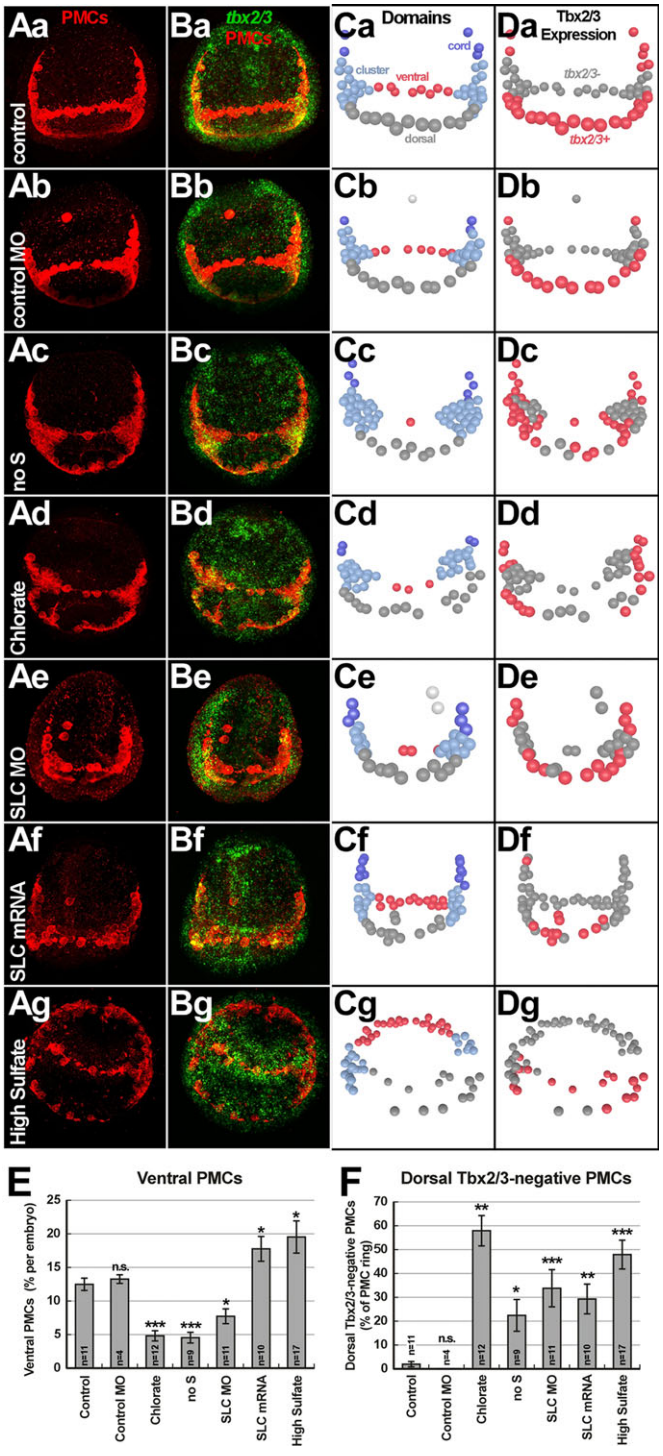

Fig. 4. SPGs are necessary and sufficient to attract PMCs ventrally. (A,B) Localization of PMCs (A,B; red) and dorsal Tbx2/3 expression (B; green) is shown in late gastrula stage embryos with the indicated treatments. (C,D) PMC models reflecting 3D coordinates extracted from image data and Tbx2/3 expression scores are shown to depict the PMC domains (C) and Tbx2/3 expression within the PMCs (D). (E,F) Quantitation of the fraction of ventral PMCs (E) and the fraction of dorsal ring Tbx2/3-negative PMCs per embryo (F), shown as mean percentages±s.e.m.; two-tailed Student's *t*-test **P*<0.05, ***P*<0.01, ****P*<0.001, n.s., not significant compared with control.

Development (2016) 143, 703-714 doi:10.1242/dev.129312

Skeletal patterning defects downstream from SPG perturbation do not reflect inhibition of VEGF signaling

To determine whether SPG perturbations impact the expression of genes implicated in skeletal patterning, we performed qPCR analysis of LG stage embryos with our suite of perturbations (Fig. S8). Of these, LvPax2/5/8 expression was upregulated only by sulfur-free ASW, whereas changes in expression of LvWnt5a and LvUnivin were below the threshold for significance (Fig. S8). However, the expression of LvVEGF and LvVEGFR was increased by several of the perturbations (Fig. S8). VEGF is an ectodermally expressed signal and VEGFR is expressed by the PMCs, implicating VEGF signaling as a patterning cue (Duloquin et al., 2007; Adomako-Ankomah and Ettensohn, 2013). Spatially, *vegf* expression appeared similar to controls in SLC MO and SLC mRNA embryos, but was increased by no-sulfur, chlorate and increased sulfate (Fig. 5A). *vegf* expression appears to be ventrally expanded in chlorate embryos (Fig. 5Ac), despite the lack of ventral PMC migration in these embryos (Fig. 4). *vegfr* expression showed a similar profile, appearing normal in SLC perturbants, but abnormal in chemical perturbants, with chlorate and no-sulfur treatments compressing *vegfr* to the PMC clusters, and increased sulfate expanding *vegfr* to the PMC ring (Fig. 5B). It is possible that the differences between the SLC perturbants and the chemical perturbants reflect the extent of penetrance of their effects.

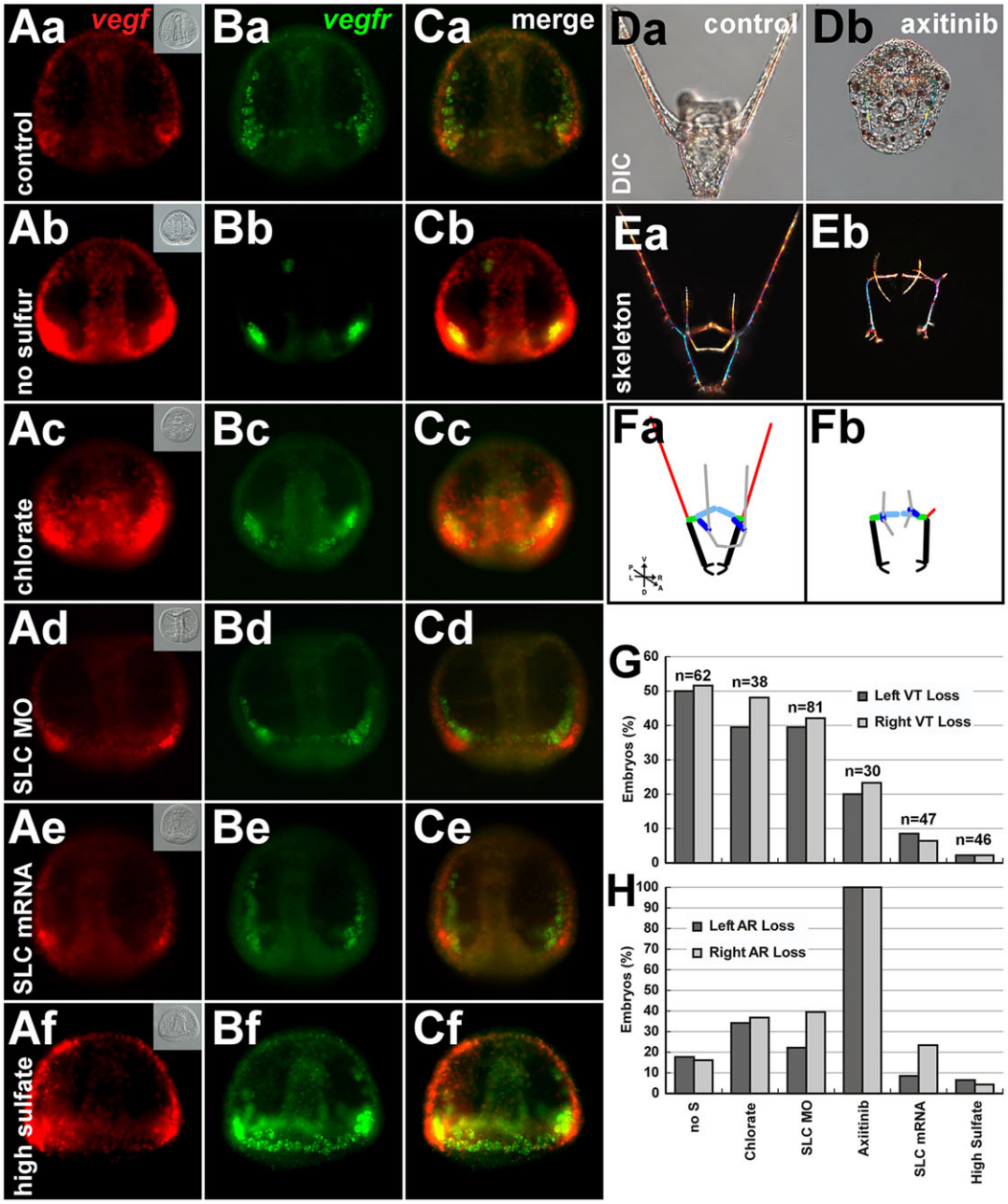

Fig. 5. SPG perturbations elicit skeletal patterning defects that are distinct from VEGF inhibition. (A-C) Expression of *vegf* (A, red) and *vegfr* (B, green) is shown in late gastrula stage control embryos and in embryos following the indicated SLC/SPG perturbations. qPCR results are shown in Fig. S8. (D-F) Morphology (D), skeletal patterns (E) and schematics (F) for control plutei (Da,Ea,Fa) and plutei developed from embryos treated with axitinib at 16 hpf (Db,Eb, Fb). The schematics emphasize the anal rods (ARs, red). (G,H) Skeleton scoring analysis scores comparing SLC/SPG perturbations with axitinib treatment are shown for the VTs (G) and the ARs (H). Complete scoring results are shown in Fig. S7D,E.

Development (2016) 143, 703-714 doi:10.1242/dev.129312

LvSlc26a2/7 is unlikely to encode the sole sulfate transporter in the embryo; therefore, chemical perturbations probably have more broad-ranging effects than molecular perturbation of a single sulfate transporter. For example, sulfur-free sea water should block entry of all sulfur and chlorate should block all PG sulfation; thus, each is likely to produce a stronger effect than SLC MO.

Increased VEGF expression levels likely indicate a compensatory response to inhibition of VEGF signaling (Adomako-Ankomah and Ettensohn, 2013), suggesting that VEGF signaling requires SPGs. Because SPGs are well known to function as signal transduction co-receptors (Baeg and Perrimon, 2000; Sarrazin et al., 2011), we tested the possibility that SPGs are required for VEGF signaling by comparing the patterning defects induced by SLC/SPG LOF and VEGFR LOF, using the VEGFR inhibitor axitinib (Bhargava and Robinson, 2011). Axitinib treatment at time points prior to 16 hpf blocked skeletogenesis; we therefore exposed embryos to axitinib at 16 hpf, then scored their skeletal defects at pluteus stage (Fig. 5D-F). Axitinib induced an overlapping yet distinct profile of skeletal patterning defects in comparison to SLC/SPG perturbation. Although it inhibited VTs in approximately 20% of embryos, midway between the effects of SLC/SPG loss and gain (Fig. 5G), axitinib did not induce midline defects, unlike SLC/SPG perturbants (Fig. S7E). Unlike SLC/SPG perturbations, axitinib strongly impacted the anal rods (ARs) (Fig. 5Fa, red elements), which were absent in 100% of axitinib-treated embryos, but more modestly impacted by SLC/SPG perturbation (Fig. 5Fb,H). This finding is in good agreement with previous studies (Adomako-Ankomah and Ettensohn, 2013). Axitinib also provoked frequent misorientation of the body rods (BRs), such that they were approximately parallel, rather than converging at the dorsal apex (Fig. 5D-F, black elements). This reflects an anterior-posterior (AP) rotation defect (Fig. S7C), which is the only orientation defect observed in axitinib-treated embryos. By contrast, parallel BRs were observed only rarely with SLC/SPG perturbations, which provoke a range of orientation defects (Fig. S7E). Thus, in multiple respects, the skeletal patterning defects in SLC/SPG perturbants are distinct from those induced by axitinib. In contrast to these differences, axitinib and SLC/SPG LOF provoked similar losses of the anterior secondary elements (the ORs and RRs) (Fig. S7D). These results indicate that loss of VEGF signaling does not account for the SLC/SPG perturbation-induced ventral skeletal patterning defects, although SPGs and VEGF might cooperate in patterning the anterior secondary skeleton.

DISCUSSION

In this study, we hypothesized that nickel and SB mutually regulate at least a subset of ectodermal skeletal patterning genes, and that this could be a basis for discriminating that subset of genes from DV specification genes, which we predicted to be reciprocally regulated by nickel and SB (Fig. 1). We identified such mutually regulated candidate genes and functionally tested them. Since all of the tested candidates provoked skeletal patterning defects upon their LOF, the results demonstrate that our hypothesis was supported. We present several novel, validated skeletal patterning genes and a wealth of untested candidates to pursue in future studies (Fig. 2). We also demonstrate that the sulfate transporter LvSLC26a2/7 is required to establish ventral SPG accumulation during gastrulation, to attract PMCs ventrally, and for development of the VT skeletal rods (Figs 3 and 4). We observed similar inhibition of PMC migration and VT development by blocking either sulfur uptake with sulfur-free sea water or proteoglycan sulfation with chlorate. Conversely, SLC overexpression or high-sulfate treatment led to increased global SPGs, excessive ventral PMC migration and, in some cases, the production of extra VTs. The reciprocal effects of these perturbations on ventral PMC attraction and skeletal patterning strengthen the conclusion that SLC-dependent SPGs provide a cue that directs PMCs ventrally and patterns the ventral transverse skeletal elements.

Previous studies have shown that manipulating the number of PMCs within the embryo has no effect on skeletal patterning, such that a substantially increased complement of PMCs migrates to the normal ring-and-cords arrangement and produces a normal skeleton, along which the PMCs are distributed more densely (Ettensohn, 1990). Furthermore, a 50% reduction in PMC number does not perturb their organization into the ring-and-cords pattern (Ettensohn, 1990). The results herein might appear to contradict that finding, since we demonstrate that reduced numbers of ventral PMCs result in the loss of the ventral skeletal elements. However, these are two quite different conditions. In the earlier studies, the ectoderm was not perturbed, and a normal set of patterning cues was presumably presented to an abnormally large or small population of otherwise normal PMCs (Ettensohn, 1990). In this study, an ectodermal patterning cue was perturbed, and a normal number of PMCs underwent abnormal migration in response, and failed both to fully occupy the ventral PMC ring and to produce ventral skeletal rods.

Sulfated proteoglycans are crucial regulators of signaling and cell migration during development (Iozzo and Schaefer, 2015) and metastasis (Cattaruzza and Perris, 2005; Theocharis et al., 2010). In some cases, SPGs function by presenting signaling ligands to their receptors. For example, in the zebrafish lateral line primordium, SPGs promote FGF signaling during collective cell migration (Venero Galanternik et al., 2015). In other cases, SPG receptors directly bind SPGs to regulate cell migration (Lang et al., 2015; Neill et al., 2015). In sea urchin embryos, SPGs have been previously implicated as regulators of PMC migration *in vitro* and *in vivo* (Karp and Solursh, 1974; Katow and Solursh, 1981; Katow, 1986; Solursh et al., 1986; Solursh and Lane, 1988), and as regulators of skeletal patterning (Sakuma et al., 2011). These results corroborate our findings, which independently identify SLC-dependent SPGs as a ventral skeletal patterning cue via an unbiased screen.

The sea urchin sulfatase HpSulf, although lacking a GOF effect alone, suppresses the radializing effects of VEGF overexpression, suggesting that SPGs facilitate VEGF signaling (Fujita et al., 2010). VEGF signals locally in sea urchin embryos (Duloquin et al., 2007), consistent with SPGs spatially retaining VEGF through direct binding. Our results suggest that SPGs and VEGF cooperate during secondary sea urchin skeletal patterning, although their functions do not completely overlap. It seems likely that the primary VT elements are patterned by SPGs in a VEGF-independent manner (Fig. 6), because inhibition of VEGFR does not strongly impact the VTs or midline and VEGF expression does not normally coincide spatially with the VTs (Fig. 5). However, VEGFR and SPG inhibition each impair anterior secondary skeletal patterning (Fig. 5, Fig. S7), as does inhibition of LvUnivin (Piacentino et al., 2015). It thus seems likely that SPGs, VEGF and Univin cooperate to direct secondary PMC migration (Fig. 6). VEGF knockdown increases VEGF expression in an apparently compensatory response (Adomako-Ankomah and Ettensohn, 2013). Such a feedback circuit would minimally involve a second signal downstream from VEGFR in the PMCs back to the ectoderm that normally functions to dampen VEGF expression. Thus, the elevated VEGF expression levels provoked by chlorate or no sulfur imply a loss of VEGF signaling and suggest that SPGs are required for VEGF signaling.

Development (2016) 143, 703-714 doi:10.1242/dev.129312

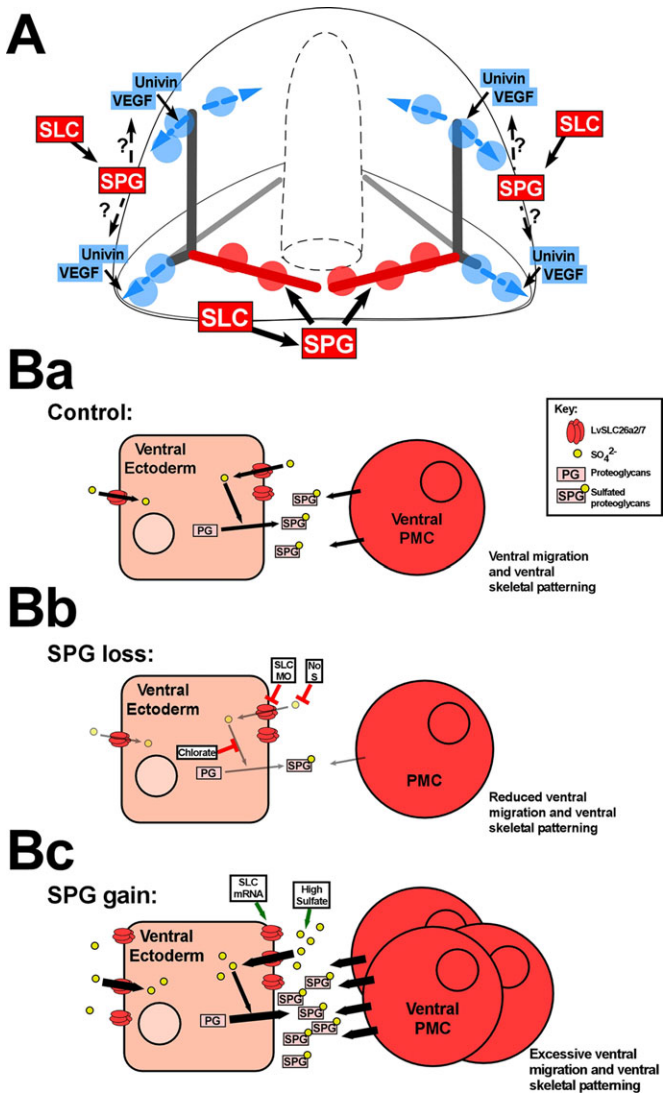

Fig. 6. Model for SLC-mediated skeletal patterning. (A) In gastrulating embryos, SLC mediates the ventral accumulation of SPGs, which, in turn, are necessary for the ventral positioning of PMCs and subsequent formation of the primary ventral transverse rods (red). Anterolateral SPGs might function to coordinate the presentation of laterally expressed Univin and VEGF signaling ligands to nearby PMCs to induce their secondary migration (blue). (B) Schematic representation of the function of SLC and SPGs at the cellular level in ventral PMC attraction in control (Ba), SPG loss (Bb) and SPG gain (Bc) conditions.

Interestingly, treatment with high sulfate also elevated VEGF expression, similarly implying that VEGF signaling is inhibited. Obtaining similar results with both SPG gain and loss could reflect a scaffolding function for SPGs, in which they jointly present VEGF and a second required factor to solicit VEGF signaling. In the absence of SPGs, the signal and factor would not be co-presented, whereas excessive SPGs levels could bind the signal and factor independently, and fail to co-present them. Because VEGF, Univin and SPGs are required for secondary skeletal patterning, we hypothesize that SPGs scaffold VEGF and Univin, co-presenting them to the PMCs to promote their secondary migration (Fig. 6).

We also found that SPG loss suppresses Tbx2/3 expression in the dorsal PMCs (Fig. 4). This result might imply that the Tbx-negative PMCs did not migrate ventrally in the perturbed embryos, and instead occupied the dorsal ring. However, SPG gain also suppressed dorsal Tbx2/3 expression while concomitantly increasing the number of ventral Tbx-negative PMCs, arguing against that conclusion. Our results show that dorsal Tbx2/3 expression requires ventral SPGs but is also suppressed by their excess (Fig. 4), again suggesting a scaffolding role for ventral SPGs in mediating dorsal Tbx2/3 expression in the PMCs. This is an unexpected result, since the known ectodermal Tbx2/3 inducers are dorsal genes or signals (Su et al., 2009; Saudemont et al., 2010); however, little is known about the regulation of PMC-specific Tbx2/3 expression. We note that inhibition of ventral specification in *L. variegatus* embryos results in radial Tbx2/3 expression (data herein and Piacentino et al., 2015), suggesting that ventral signals locally suppress Tbx2/3 expression, which is otherwise globally induced.

This study identifies novel ectodermal cues for patterning the sea urchin larval skeleton, and for the first time, identifies a cue required to pattern a specific element of the primary skeleton. It will be interesting to extend this study to our additional candidates and to further unravel the basis for sea urchin skeletal patterning.

MATERIALS AND METHODS

Animals, perturbations, surgeries, imaging and skeletal scoring

Adult *Lytechinus variegatus* sea urchins were obtained from the Duke University Marine Laboratory (Beaufort, NC) or from Reeftopia (Miami, FL). Gamete harvesting, embryo culturing and microinjection were performed as described (Bradham and McClay, 2006). See supplementary Materials and Methods and Table S3 for additional details. Microsurgeries to produce chimeras were performed as described (Armstrong et al., 1993). Larval skeletons were imaged in multiple focal planes, which were manually recombined into montage images using Canvas (ACD Systems) to present complete larval skeleton in focus, for clarity. The full set of skeletal images was used for scoring, as described in Fig. S7.

RNA-Seq, data assembly and analysis

Total RNA was polyA selected, then cDNA libraries were prepared and sequenced on an Illumina GAII platform. 101 bp paired-end reads were initially assembled using SOAPdenovo (Li et al., 2010), and finally assembled using SOAPdenovo-Trans (Xie et al., 2014). Transcriptome assembly and annotation will be described elsewhere and are available at NCBI (BioProject accession number PRJNA241187; J. D. Hogan, J.L.K., L.L., E.E.S., A. Saji, M. A. Sundermeyer, D. Schatzberg, M.L.P., D.T.Z., A.B.C., C. Blumberg, J.I.-S., B. Timmerman, J. G. Grau, N. Irie, A.J.P. and C.A.B., unpublished data). Differential analysis was performed using DESeq (Anders and Huber, 2010). MA plots were generated in R (R Core Team, 2014). GO term enrichment analysis was performed with iPAGE (Goodarzi et al., 2009) and metabolic maps were generated with iPath 2.0 (Yamada et al., 2011).

Whole-mount *in situ* hybridization

Full-length riboprobes were labeled with DNP-11-UTP (PerkinElmer) or digoxigenin (DIG, Roche). *In situ* hybridization was performed as described (Bradham et al., 2009; Piacentino et al., 2015).

Immunostaining and confocal microscopy

Immunolabeling was performed as described (Bradham and McClay, 2006; Piacentino et al., 2015). Primary antibodies include PMC-specific 6a9 (1:5; from Charles Ettensohn, Carnegie Mellon University, Pittsburgh, PA, USA) and ciliary band-specific 295 (undiluted; from David McClay, Duke University, Durham, NC, USA). Secondary antibodies were goat anti-mouse Cy3 (1:500; Jackson Laboratories) and goat anti-mouse Alexa Fluor 488 (1:500; Molecular Probes). All images are full projections of *z*-stacks.

3D PMC modeling and analysis

ImageJ was used to manually process confocal *z*-stack images and to define the center of each PMC using the multi-point ROI manager; LvTbx2/3 expression was manually scored for each PMC. ROI sets were mapped to 3D

space using Blender 2.75 (www.blender.org). For domain assignments, PMCs were defined as belonging to a cluster if they contacted more than two other PMCs.

Alcian Blue histochemistry

Sea urchin embryos were fixed in 2.5% glutaraldehyde (Polysciences) and 0.025 M sodium cacodylate (Sigma) in ASW for approximately 24 h, then washed into staining solution containing 0.3 M magnesium chloride (MP Biomedicals) and 0.05% Alcian Blue cationic dye (Sigma) at pH 2.5 to specifically label sulfated functional groups (Scott and Dorling, 1965). After 24 h in staining solution, embryos were washed and imaged. See supplementary Materials and Methods for details on image processing and quantitation, and for the Cuprolinic staining method.

qPCR analysis

qPCR analysis was performed as described (Piacentino et al., 2015). qPCR primer sequences are provided in Table S4.

Acknowledgements

We thank Dave McClay for antibodies and help with chimeras, Chuck Ettensohn for antibodies, Yi-Hsien Su and Smadar Ben-Tabou de-Leon for helpful technical advice, Gary Benson for Bioinformatics Challenge and Database Projects course leadership and John C. Celenza for helpful discussions.

Competing interests

The authors declare no competing or financial interests.

Author contributions

C.A.B. conceived of the study. E.E.S., J.D.H., J.L.K., L.L., J.C.-H., J.I.-S., A.J.P. and C.A.B. performed bioinformatics analyses. M.L.P., D.T.Z., J.F., S.R., C.L., J.Y., O.C., J.R., P.F., V.P., A.R., H.H., J.C., F.B.H., E.B., D.L., A.B.C., T.A.B., E.O. and C.A.B. performed biological analyses. M.L.P. and C.A.B. wrote the manuscript.

Funding

This work was supported by the National Science Foundation (NSF) [IOS 950030254 to C.A.B.]; and start-up funds from Boston University (to C.A.B.). J.H.-C. was supported by a National Science and Engineering Research Council of Canada Fellowship. J.F., O.C., P.F., V.P., and A.R. were partially supported by fellowships from the Boston University Undergraduate Research Opportunities Program.

Supplementary information

Supplementary information available online at
http://dev.biologists.org/lookup/suppl/doi:10.1242/dev.129312/-/DC1

References

Adomako-Ankomah, A. and Ettensohn, C. A. (2013). Growth factor-mediated mesodermal cell guidance and skeletogenesis during sea urchin gastrulation. *Development* **140**, 4214-4225.

Adomako-Ankomah, A. and Ettensohn, C. A. (2014). Growth factors and early mesoderm morphogenesis: insights from the sea urchin embryo. *Genesis* **52**, 158-172.

Anders, S. and Huber, W. (2010). Differential expression analysis for sequence count data. *Genome Biol.* **11**, R106.

Angerer, L. M., Oleksyn, D. W., Logan, C. Y., McClay, D. R., Dale, L. and Angerer, R. C. (2000). A BMP pathway regulates cell fate allocation along the sea urchin animal-vegetal embryonic axis. *Development* **127**, 1105-1114.

Armstrong, N., Hardin, J. and McClay, D. R. (1993). Cell-cell interactions regulate skeleton formation in the sea urchin embryo. *Development* **119**, 833-840.

Baeg, G.-H. and Perrimon, N. (2000). Functional binding of secreted molecules to heparan sulfate proteoglycans in Drosophila. *Curr. Opin. Cell Biol.* **12**, 575-580.

Baeuerle, P. A. and Huttner, W. B. (1986). Chlorate–a potent inhibitor of protein sulfation in intact cells. *Biochem. Biophys. Res. Commun.* **141**, 870-877.

Barsi, J. C., Li, E. and Davidson, E. H. (2015). Geometric control of ciliated band regulatory states in the sea urchin embryo. *Development* **142**, 953-961.

Bergeron, K.-F., Xu, X. and Brandhorst, B. P. (2011). Oral–aboral patterning and gastrulation of sea urchin embryos depend on sulfated glycosaminoglycans. *Mech. Dev.* **128**, 71-89.

Bhargava, P. and Robinson, M. O. (2011). Development of second-generation VEGFR tyrosine kinase inhibitors: current status. *Curr. Oncol. Rep.* **13**, 103-111.

Bradham, C. A. and McClay, D. R. (2006). p38 MAPK is essential for secondary axis specification and patterning in sea urchin embryos. *Development* **133**, 21-32.

Bradham, C. A., Oikonomou, C., Kühn, A., Core, A. B., Modell, J. W., McClay, D. R. and Poustka, A. J. (2009). Chordin is required for neural but not axial development in sea urchin embryos. *Dev. Biol.* **328**, 221-233.

Cattaruzza, S. and Perris, R. (2005). Proteoglycan control of cell movement during wound healing and cancer spreading. *Matrix Biol.* **24**, 400-417.

Cavalieri, V., Spinelli, G. and Di Bernardo, M. (2003). Impairing Otp homeodomain function in oral ectoderm cells affects skeletogenesis in sea urchin embryos. *Dev. Biol.* **262**, 107-118.

Cavalieri, V., Guarcello, R. and Spinelli, G. (2011). Specific expression of a TRIM-containing factor in ectoderm cells affects the skeletal morphogenetic program of the sea urchin embryo. *Development* **138**, 4279-4290.

Chan, F. L., Inoue, S. and Leblond, C. P. (1992). Localization of heparan sulfate proteoglycan in basement membrane by side chain staining with cuprolinic blue as compared with core protein labeling with immunogold. *J. Histochem. Cytochem.* **40**, 1559-1572.

Croce, J., Lhomond, G. and Gache, C. (2003). Coquillette, a sea urchin T-box gene of the Tbx2 subfamily, is expressed asymmetrically along the oral–aboral axis of the embryo and is involved in skeletogenesis. *Mech. Dev.* **120**, 561-572.

Davies, S. P., Reddy, H., Caivano, M. and Cohen, P. (2000). Specificity and mechanism of action of some commonly used protein kinase inhibitors. *Biochem. J.* **351**, 95-105.

Di Bernardo, M., Castagnetti, S., Bellomonte, D., Oliveri, P., Melfi, R., Palla, F. and Spinelli, G. (1999). Spatially restricted expression of PlOtp, a Paracentrotus lividus orthopedia-related homeobox gene, is correlated with oral ectodermal patterning and skeletal morphogenesis in late-cleavage sea urchin embryos. *Development* **126**, 2171-2179.

Duboc, V., Röttinger, E., Besnardeau, L. and Lepage, T. (2004). Nodal and BMP2/4 signaling organizes the oral-aboral axis of the sea urchin embryo. *Dev. Cell* **6**, 397-410.

Duloquin, L., Lhomond, G. and Gache, C. (2007). Localized VEGF signaling from ectoderm to mesenchyme cells controls morphogenesis of the sea urchin embryo skeleton. *Development* **134**, 2293-2302.

Ettensohn, C. A. (1990). The regulation of primary mesenchyme cell patterning. *Dev. Biol.* **140**, 261-271.

Flowers, V. L., Courteau, G. R., Poustka, A. J., Weng, W. and Venuti, J. M. (2004). Nodal/activin signaling establishes oral-aboral polarity in the early sea urchin embryo. *Dev. Dyn.* **231**, 727-740.

Forlino, A., Piazza, R., Tiveron, C., Della Torre, S., Tatangelo, L., Bonafè, L., Gualeni, B., Romano, A., Pecora, F., Superti-Furga, A. et al. (2005). A diastrophic dysplasia sulfate transporter (SLC26A2) mutant mouse: morphological and biochemical characterization of the resulting chondrodysplasia phenotype. *Hum. Mol. Genet.* **14**, 859-871.

Fujita, K., Takechi, E., Sakamoto, N., Sumiyoshi, N., Izumi, S., Miyamoto, T., Matsuura, S., Tsurugaya, T., Akasaka, K. and Yamamoto, T. (2010). HpSulf, a heparan sulfate 6-O-endosulfatase, is involved in the regulation of VEGF signaling during sea urchin development. *Mech. Dev.* **127**, 235-245.

Goodarzi, H., Elemento, O. and Tavazoie, S. (2009). Revealing global regulatory perturbations across human cancers. *Mol. Cell* **36**, 900-911.

Gross, J. M., Peterson, R. E., Wu, S.-Y. and McClay, D. R. (2003). LvTbx2/3: a T-box family transcription factor involved in formation of the oral/aboral axis of the sea urchin embryo. *Development* **130**, 1989-1999.

Gualeni, B., Facchini, M., De Leonardis, F., Tenni, R., Cetta, G., Viola, M., Passi, A., Superti-Furga, A., Forlino, A. and Rossi, A. (2010). Defective proteoglycan sulfation of the growth plate zones causes reduced chondrocyte proliferation via an altered Indian hedgehog signalling. *Matrix Biol.* **29**, 453-460.

Gustafson, T. and Wolpert, L. (1999). Studies on the cellular basis of morphogenesis in the sea urchin embryo. Directed movements of primary mesenchyme cells in normal and vegetalized larvae. *Exp. Cell Res.* **253**, 288-295.

Hardin, J., Coffman, J. A., Black, S. D. and McClay, D. R. (1992). Commitment along the dorsoventral axis of the sea urchin embryo is altered in response to NiCl2. *Development* **116**, 671-685.

Iozzo, R. V. and Schaefer, L. (2015). Proteoglycan form and function: a comprehensive nomenclature of proteoglycans. *Matrix Biol.* **42**, 11-55.

Karp, G. C. and Solursh, M. (1974). Acid mucopolysaccharide metabolism, the cell surface, and primary mesenchyme cell activity in the sea urchin embryo. *Dev. Biol.* **41**, 110-123.

Katow, H. (1986). Behavior of sea urchin primary mesenchyme cells in artificial extracellular matrices. *Exp. Cell Res.* **162**, 401-410.

Katow, H. and Solursh, M. (1981). Ultrastructural and time-lapse studies of primary mesenchyme cell behavior in normal and sulfate-deprived sea urchin embryos. *Exp. Cell Res.* **136**, 233-245.

Lang, B. T., Cregg, J. M., DePaul, M. A., Tran, A. P., Xu, K., Dyck, S. M., Madalena, K. M., Brown, B. P., Weng, Y.-L., Li, S. et al. (2015). Modulation of the proteoglycan receptor PTPsigma promotes recovery after spinal cord injury. *Nature* **518**, 404-408.

Lapraz, F., Besnardeau, L. and Lepage, T. (2009). Patterning of the dorsal-ventral axis in echinoderms: insights into the evolution of the BMP-chordin signaling network. *PLoS Biol.* **7**, e1000248.

Li, R., Zhu, H., Ruan, J., Qian, W., Fang, X., Shi, Z., Li, Y., Li, S., Shan, G., Kristiansen, K. et al. (2010). De novo assembly of human genomes with massively parallel short read sequencing. *Genome Res.* **20**, 265-272.

Lyons, D. C., Kaltenbach, S. L. and McClay, D. R. (2012). Morphogenesis in sea urchin embryos: linking cellular events to gene regulatory network states. *Wiley Interdiscip. Rev. Dev. Biol.* **1**, 231-252.
McIntyre, D. C., Seay, N. W., Croce, J. C. and McClay, D. R. (2013). Short-range Wnt5 signaling initiates specification of sea urchin posterior ectoderm. *Development* **140**, 4881-4889.
McIntyre, D. C., Lyons, D. C., Martik, M. and McClay, D. R. (2014). Branching out: origins of the sea urchin larval skeleton in development and evolution. *Genesis* **52**, 173-185.
Miller, J., Fraser, S. E. and McClay, D. (1995). Dynamics of thin filopodia during sea urchin gastrulation. *Development* **121**, 2501-2511.
Mount, D. B. and Romero, M. F. (2004). The SLC26 gene family of multifunctional anion exchangers. *Pfluegers Arch.* **447**, 710-721.
Neill, T., Schaefer, L. and Iozzo, R. V. (2015). Decoding the matrix: instructive roles of proteoglycan receptors. *Biochemistry* **54**, 4583-4598.
Piacentino, M. L., Ramachandran, J. and Bradham, C. A. (2015). Late Alk4/5/7 signaling is required for anterior skeletal patterning in sea urchin embryos. *Development* **142**, 943-952.
R Core Team (2014). *R: A Language and Environment for Statistical Computing*. Vienna, Austria: R Foundation for Statistical Computing.
Rossi, A., Kaitila, I., Wilcox, W. R., Rimoin, D. L., Steinmann, B., Cetta, G. and Superti-Furga, A. (1998). Proteoglycan sulfation in cartilage and cell cultures from patients with sulfate transporter chondrodysplasias: relationship to clinical severity and indications on the role of intracellular sulfate production. *Matrix Biol.* **17**, 361-369.
Rottinger, E., Saudemont, A., Duboc, V., Besnardeau, L., McClay, D. and Lepage, T. (2008). FGF signals guide migration of mesenchymal cells, control skeletal morphogenesis [corrected] and regulate gastrulation during sea urchin development. *Development* **135**, 353-365.
Sakuma, T., Ohnishi, K., Fujita, K., Ochiai, H., Sakamoto, N. and Yamamoto, T. (2011). HpSumf1 is involved in the activation of sulfatases responsible for regulation of skeletogenesis during sea urchin development. *Dev. Genes Evol.* **221**, 157-166.
Sarrazin, S., Lamanna, W. C. and Esko, J. D. (2011). Heparan sulfate proteoglycans. *Cold Spring Harb. Perspect. Biol.* **3**, a004952.
Saudemont, A., Haillot, E., Mekpoh, F., Bessodes, N., Quirin, M., Lapraz, F., Duboc, V., Röttinger, E., Range, R., Oisel, A. et al. (2010). Ancestral regulatory circuits governing ectoderm patterning downstream of Nodal and BMP2/4 revealed by gene regulatory network analysis in an echinoderm. *PLoS Genet.* **6**, e1001259.
Scott, J. E. and Dorling, J. (1965). Differential staining of acid glycosaminoglycans (mucopolysaccharides) by alcian blue in salt solutions. *Histochemie* **5**, 221-233.
Solursh, M. and Lane, M. C. (1988). Extracellular matrix triggers a directed cell migratory response in sea urchin primary mesenchyme cells. *Dev. Biol.* **130**, 397-401.
Solursh, M., Mitchell, S. L. and Katow, H. (1986). Inhibition of cell migration in sea urchin embryos by beta-D-xyloside. *Dev. Biol.* **118**, 325-332.
Su, Y.-H., Li, E., Geiss, G. K., Longabaugh, W. J. R., Krämer, A. and Davidson, E. H. (2009). A perturbation model of the gene regulatory network for oral and aboral ectoderm specification in the sea urchin embryo. *Dev. Biol.* **329**, 410-421.
Tan, H., Ransick, A., Wu, H., Dobias, S., Liu, Y.-H. and Maxson, R. (1998). Disruption of primary mesenchyme cell patterning by misregulated ectodermal expression of SpMsx in sea urchin embryos. *Dev. Biol.* **201**, 230-246.
Theocharis, A. D., Skandalis, S. S., Tzanakakis, G. N. and Karamanos, N. K. (2010). Proteoglycans in health and disease: novel roles for proteoglycans in malignancy and their pharmacological targeting. *FEBS J.* **277**, 3904-3923.
Tu, Q., Cameron, R. A. and Davidson, E. H. (2014). Quantitative developmental transcriptomes of the sea urchin Strongylocentrotus purpuratus. *Dev. Biol.* **385**, 160-167.
van Heijster, P., Hardway, H., Kaper, T. J. and Bradham, C. A. (2014). A computational model for BMP movement in sea urchin embryos. *J. Theor. Biol.* **363**, 277-289.
Venero Galanternik, M., Kramer, K. L. and Piotrowski, T. (2015). Heparan sulfate proteoglycans regulate Fgf signaling and cell polarity during collective cell migration. *Cell Rep.* **10**, 414-428.
von Ubisch, L. (1937). Di Normale Skelettbildung bei Echinocyamus pusillus und Psamechinus miliaris und die Bedeutung dieser Vorgänge für die Analyse der Skelette von Keimblatt-Chimären. *Z Wiss. Zool.* **149**, 402-476.
Wilt, F., Killian, C. E., Croker, L. and Hamilton, P. (2013). SM30 protein function during sea urchin larval spicule formation. *J. Struct. Biol.* **183**, 199-204.
Xie, Y., Wu, G., Tang, J., Luo, R., Patterson, J., Liu, S., Huang, W., He, G., Gu, S., Li, S. et al. (2014). SOAPdenovo-Trans: de novo transcriptome assembly with short RNA-Seq reads. *Bioinformatics* **30**, 1660-1666.
Yaguchi, S., Yaguchi, J., Angerer, R. C., Angerer, L. M. and Burke, R. D. (2010). TGFbeta signaling positions the ciliary band and patterns neurons in the sea urchin embryo. *Dev. Biol.* **347**, 71-81.
Yamada, T., Letunic, I., Okuda, S., Kanehisa, M. and Bork, P. (2011). iPath2.0: interactive pathway explorer. *Nucleic Acids Res.* **39**, W412-W415.

SUPPLEMENTARY MATERIALS AND METHODS

Embryo perturbation and imaging details

MOs were purchased from Gene Tools; their sequences are listed in Figure S2. The sequence of the control MO is 5'-AGTAGACGAGCTTGTACTGAGGCAT-3'. Injected mRNAs were *in vitro* transcribed using the mMESSAGE mMACHINE kit (Ambion). For Ni and SB treatments, embryos were exposed from fertilization to mesenchyme blastula stage (0-12 hpf). Dose-response experiments were performed to determine the optimal working dose for each reagent presented in this study, and complete descriptions of dose timing and concentration ranges are described in Table S3. Each perturbation experiment was performed in at least three independent biological replicates. From each loss-of-function experiment, a large number of randomly selected plutei were imaged and scored as described in Figure S7. Exemplars were selected for presentation based on the scoring results as those that best reflected the most commonly observed defects for each perturbation. MO phenotypic penetrance data is displayed in Figure S3P.

Skeletal patterning candidate selection rationale

Candidates were selected from an initial list of 879 scaffolds whose expression level (normalized counts) was downregulated in both Ni and SB by ≥ 2-fold compared to control. Of these, 114 genes were identifiable (Table S1). 77 of these encode extracellular proteins (based on orthology), and we manually selected candidates from among this short list. LvSLC26a2/7 was selected because of its orthology to a mammalian skeletal patterning gene (Mount and Romero, 2004). LvNFL (Notch- and Fibropellin-like) was selected because of its probable adhesive functions (Bisgrove et al., 1991), which we reasoned are likely to contribute to ectodermal patterning mechanisms. LvLOX (lipoxygenase) was selected because LOX-produced HETEs regulate a range of signaling pathways (Pidgeon et al., 2007). Finally, LvBMP5-8 was selected because it is a well-known signaling ligand, and because it was upregulated by Ni and SB in the initial assembly, and therefore reflected a mutually upregulated candidate.

Candidate gene cloning, sequence, and splice analysis

Candidate gene sequence reads were used to assemble provisional gene models, which were empirically extended by RACE using FirstChoice RLM-RACE kit (Ambion). Intron positions were predicted based on corresponding intron positions in S. purpuratus ((Sodergren et al., 2006), http://www.echinobase.org), then amplified, cloned and sequenced for splice-blocking MO sequence design. Phylogenetic analysis was performed using MrBayes (http://mrbayes.sourceforge.net) and visualized using FigTree (http://tree.bio.ed/ac/uk/software/figtree/). Sequence alignment was carried out using MultAlin (Corpet, 1988). Full length LvSLC26a2/7 cDNA (GenBank accession number KR055815) was obtained by RACE, then subcloned into pCS2 for in vitro transcription, after the addition of an artificial polyA track (20mer) in the 3' UTR to enhance mRNA stability *in vivo*. LvNFL (GenBank accession number KR055816), LvBMP5-8 (GenBank accession number KT428770), and LvLOX (GenBank accession number KR055817) cDNAs were cloned using standard methods and subcloned into pCS2 for in vitro transcription. For RT-PCR splice analysis, total RNA from control, SLC MO-, NFL MO- and BMP5-8 MO-injected embryos at LG stage was collected and DNase-treated using the RNeasy Micro Kit (QIAGEN), and cDNAs were synthesized using the Transcriptor High Fidelity cDNA Synthesis Kit (Roche). Relevant primer sequences are listed in Table S4.

Alcian Blue signal quantitation and pseudocoloring, and Cuprolinic acid staining

Scoring of Alcian blue-stained embryos was restricted to embryos photographed in posterior views to optimize dorsal and ventral signal comparisons. Gray scale images were analyzed in ImageJ, which was used to select multiple regions of interest (ROIs) in the ectoderm. The average pixel intensity per unit area was determined for each ROI. Three or four independent ventral and dorsal ROIs were averaged per embryo, then their ratios were calculated. For pseudocoloring, gray scale images were generated, then a custom rainbow look up table was applied that colors pixel intensities according to the scale presented in Figures 3 and S6 using the software Canvas (ACD Systems). Fixation and Cuprolinic acid staining were simultaneously performed in 2.5% gluteraldehyde (Polysciences, Inc.) with 0.025 M sodium cacodylate (Sigma), 2.5 M $MgCl_2$ (MP Biomedicals), and 1% Cuprolinic blue cationic dye (Quinolinic phthalocyanine; Polysciences, Inc.) in ASW for approximately 90 minutes at room temperature to label sulfated proteoglycan side chains (Chan et al., 1992); embryos were then washed, imaged, and pseudocolored as described for Alcian blue.

Development • Supplementary information

Table S1

Click here to Download Table S1

Table S2

Click here to Download Table S2

Table S3. Perturbation timing and dose information

Perturbation (Vendor)	Stage (hours post fertilization, hpf)	Dose Range
$NiCl_2$ (Sigma)	Zygote to 12 hpf	0.3 mM – 0.5 mM
SB203580 (Calbiochem)	Zygote to 12 hpf	25 µM – 30 µM
LvSLC26a2/7 MO (Gene Tools)	Zygote	1.33 mM - 2.67 mM
LvSLC26a2/7 mRNA	Zygote	1.25 µg/µl – 4 µg/µl
LvNFL MO (Gene Tools)	Zygote	1 mM – 2 mM
LvNFL mRNA	Zygote	12 – 14 µg/µl
LvBMP5-8 MO (Gene Tools)	Zygote	0.5 mM – 1.33 mM
LvBMP5-8 mRNA	Zygote	0.5 – 1 µg/µl
LvLOX MO (Gene Tools)	Zygote	0.53 mM – 0.8 mM
LvLOX mRNA	Zygote	1 – 2 µg/µl
Control MO (Gene Tools)	Zygote	1 mM
Sulfur-free artificial sea water	10 hpf	0 mM magnesium sulfate
Sodium chlorate (Sigma)	10 hpf	10 mM – 30 mM
High sulfate artificial sea water	10 hpf	68 mM – 100 mM magnesium sulfate
Axitinib (Sigma)	16 hpf	25 nM

Development • Supplementary information

Table S4. Primer sequences

Primer	Sequence (5' --> 3')	Use
LvSLC26a2/7 forward	TAGATGATCGAACGGAGGACC	cloning
LvSLC26a2/7 reverse	CAATCCAATTAAGGGTTTCGAGTTGTTTGC	cloning
LvSLC26a2/7 5' UTR BamHI	atcaaggatccCAGTGCCATGGACCACTGGATTGC[a]	cloning
LvSLC26a2/7 3' UTR polyA XhoI	atatactcgagttttttttttttttttttttCACCAAGAATT ATCCCCGTCC[a]	cloning
LvSLC26a2/7 splice analysis forward (exon 13)	GTGGATCTTGGTCTTGGTGTCG	splice analysis
LvSLC26a2/7 splice analysis reverse (exon 14)	CTGTCTGAACTGCTGGGCATTGG	splice analysis
LvSLC26a2/7 splice analysis reverse (exon 16)	GGTTGCTATGCCAATCCTGTCG	splice analysis
LvNFL forward HindIII	attaagcttCCACCACCAAACCTGCCACACG[a]	cloning
LvNFL reverse XbaI	atatctagaCCCGATGTTCGGAAGTAAATTGCAGG[a]	cloning
LvNFL splice analysis forward (exon L)	ACTGGAGTCACGTGTGAGACG	splice analysis
LvNFL splice analysis reverse (exon M)	ACCATTTCGACACGGATTGC	splice analysis
LvNFL splice analysis reverse (exon O)	CACGTAGCATCAACTTGACAGG	splice analysis
LvBMP5-8 start EcoRI	ggaattcATGCTCATTTTCCCTTCAGTGATG[a]	cloning
LvBMP5-8 stop XhoI	ccgctcgagCTAAAGGCAACCACAGGCACG[a]	cloning
LvBMP5-8 splice analysis forward (exon 1)	TTGGACCAGGGCTAAGTTGG	splice analysis
LvBMP5-8 splice analysis reverse (exon 2)	GAGGTATCCTACCGATGTCG	splice analysis
LvBMP5-8 splice analysis reverse (exon 3)	CCTGAGATGGGATGAAGTCG	splice analysis
LvLOX stop XbaI	ccgtctagaTTAAATACTGATTGCATTAGGGACTTCTTTAGG[a]	cloning
LvSLC26a2/7 forward	TCCCTGTTGGATTTCCCAAAC	qPCR
LvSLC26a2/7 reverse	CACTGCAAAGCCCACAATAGC	qPCR
LvVEGF forward	CTACAAAGGAAGGCGGAACG	qPCR
LvVEGF reverse	GCTCCGTTGATACATGGTGG	qPCR
LvVEGFR forward	CCACCATCACCCATCAAACCACC	qPCR
LvVEGFR reverse	CCCTGACCTGAATCCACTGG	qPCR
LvPax2/5/8 forward	CGGCTGTTGGCCGAGGGTGTGTGC	qPCR
LvPax2/5/8 reverse	CGTCCTCTCTGGGTCTCCAGGGTG	qPCR
LvWnt5a forward	CGAGCTCTTCATCCTTGGTACA	qPCR
LvWnt5a reverse	TGGTCCTGGTAGAGCTGACATA	qPCR
LvUnivin forward	CAAATGGCAGCAACAGAAGA	qPCR
LvUnivin reverse	GGAATGGAAGCTACGTCGAA	qPCR
LvSetmar forward	GCCATCATGTCCTTGTCTCA	qPCR
LvSetmar reverse	CACATGAAGCTTGATCAGGTAGTC	qPCR

[a]Upper case indicates gene-specific sequence, while lower case indicates artificial polyA track (underlined) and restriction sites.

Development • Supplementary information

REFERENCES

Bisgrove, B. W., Andrews, M. E. and Raff, R. A. (1991) 'Fibropellins, products of an EGF repeat-containing gene, form a unique extracellular matrix structure that surrounds the sea urchin embryo', *Developmental Biology* **146**(1): 89-99.
Chan, F. L., Inoue, S. and Leblond, C. P. (1992) 'Localization of heparan sulfate proteoglycan in basement membrane by side chain staining with cuprolinic blue as compared with core protein labeling with immunogold', *Journal of Histochemistry and Cytochemistry* **40**(10): 1559-72.
Corpet, F. (1988) 'Multiple sequence alignment with hierarchical clustering', *Nucleic Acids Research* **16**(22): 10881-90.
Mount, D. B. and Romero, M. F. (2004) 'The SLC26 gene family of multifunctional anion exchangers', *Pfluegers Archiv European Journal of Physiology* **447**(5): 710-21.
Pidgeon, G. P., Lysaght, J., Krishnamoorthy, S., Reynolds, J. V., O'Byrne, K., Nie, D. and Honn, K. V. (2007) 'Lipoxygenase metabolism: roles in tumor progression and survival', *Cancer and Metastasis Reviews* **26**(3-4): 503-24.
Sodergren, E. Weinstock, G. M. Davidson, E. H. Cameron, R. A. Gibbs, R. A. Angerer, R. C. Angerer, L. M. Arnone, M. I. Burgess, D. R. Burke, R. D. et al. (2006) 'The genome of the sea urchin Strongylocentrotus purpuratus', *Science* **314**(5801): 941-52.

Development • Supplementary information

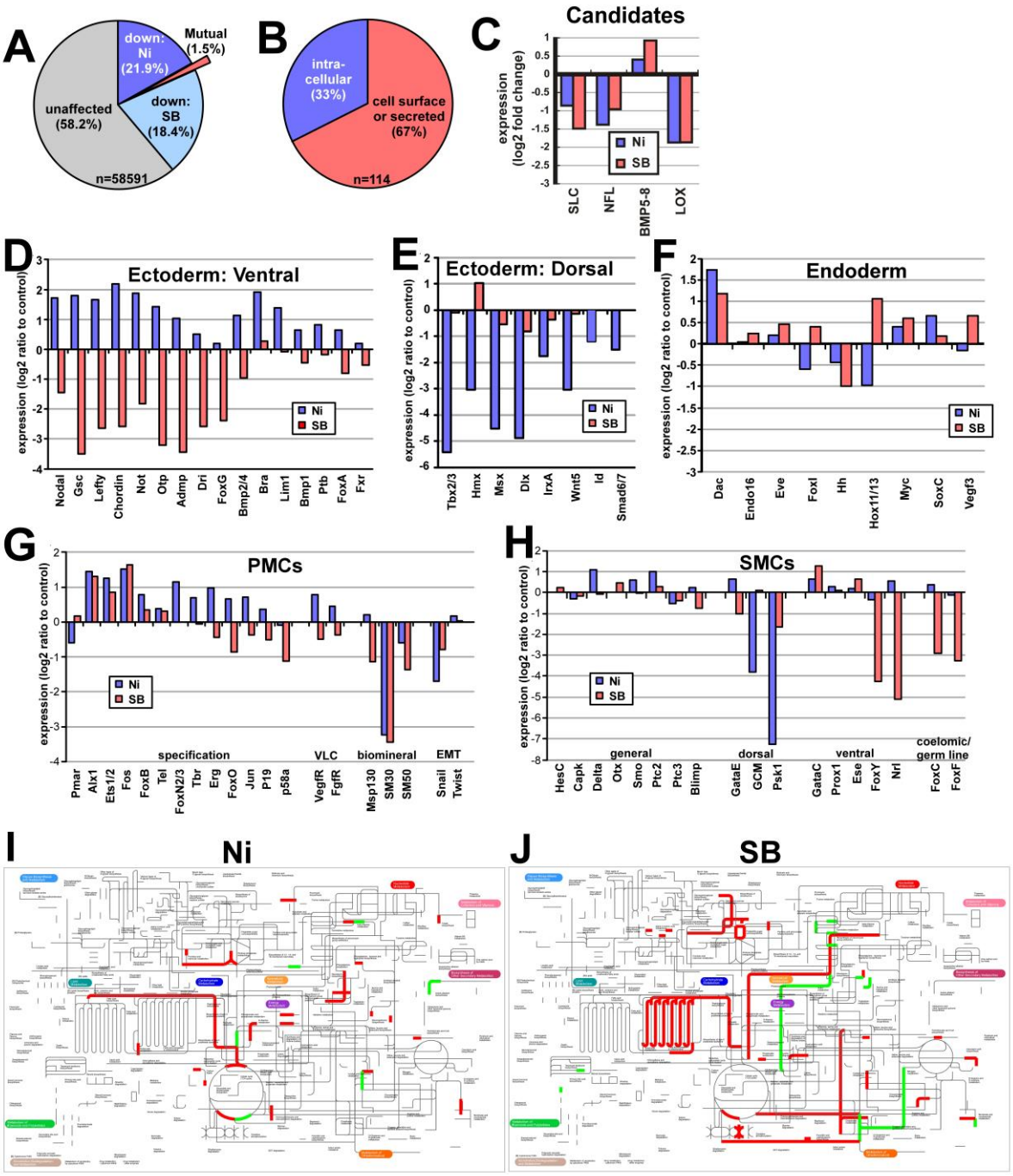

Figure S1. Identification of skeletal patterning candidates by differential analysis of RNA-Seq data and expression analysis of known specification, differentiation, and metabolic genes. A-B. Pie charts display the results of the differential expression analysis from the initial assembly. From the mutually downregulated set (A; red), the subcellular distribution of the identifiable subset is shown (B). **C.** RNA-seq expression values from the final assembly are shown relative to controls for the four candidate skeletal patterning genes described in Fig. 2. **D-H.** RNA-seq expression values from the final assembly are shown relative to controls for genes specifically expressed in the ventral ectoderm (D), the dorsal ectoderm (E), the endoderm (F), the skeletogenic primary mesenchyme cells (PMCs; G), and the secondary mesenchyme cells (SMCs; H). **I-J.** Differential RNA-seq expression values for 372 sea urchin metabolic network components were mapped using iPath 2.0. Increased (green) and decreased (red) gene expression at a 4-fold cut-off is shown for Ni (I) and SB (J) at late gastrula stage compared to controls.

Development • Supplementary information

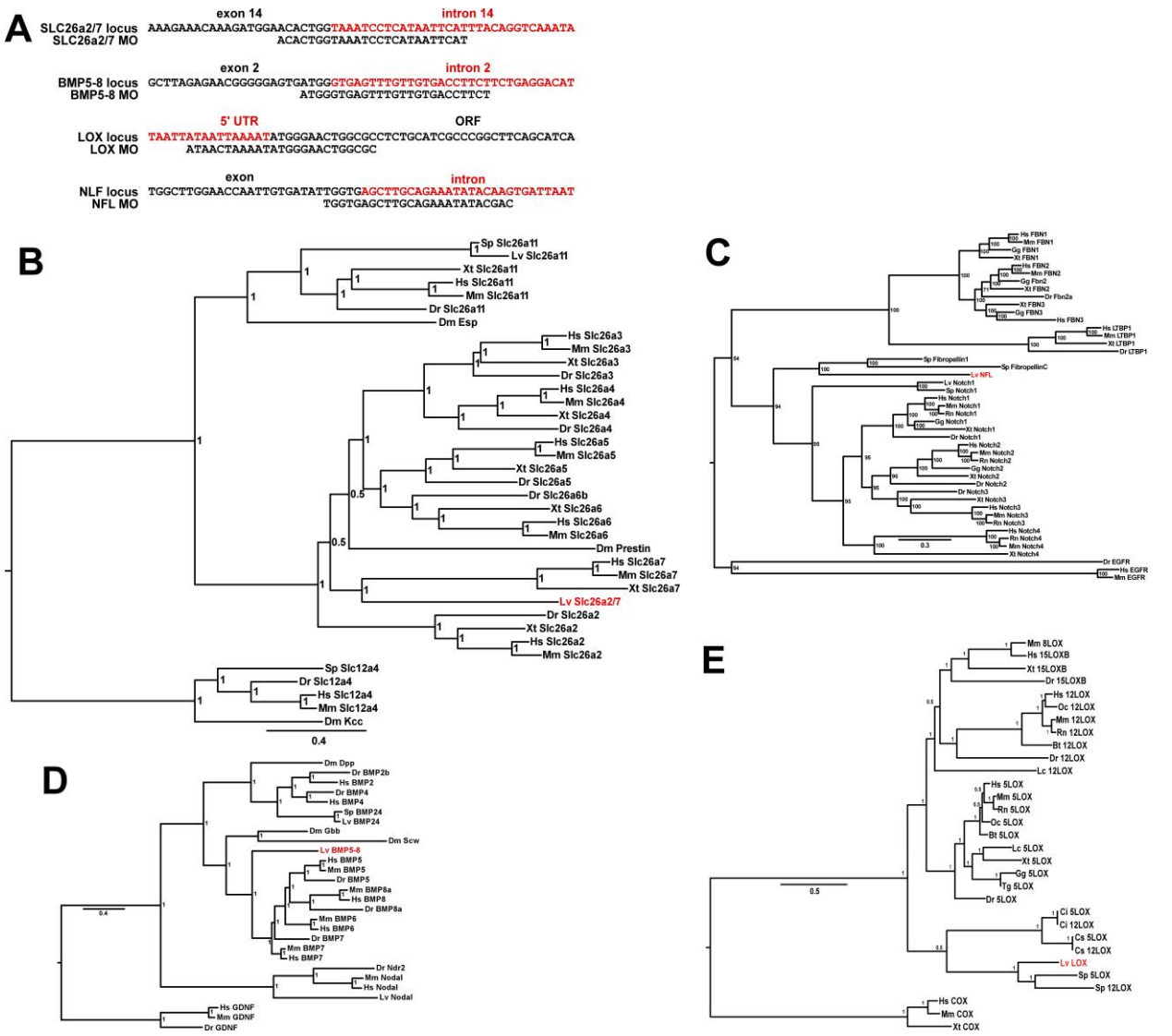

Figure S2. Morpholino design and phylogenetic analysis for four identified skeletal patterning candidate genes. A. The designs for morpholino antisense oligonucleotide (MOs) sequences are shown for six skeletal patterning candidate genes. Three MOs are designed to block mRNA splicing (SLC, BMP5-8, and NFL), while one is designed to block translation (LOX). Untranslated sequences are indicated in red. **B-E.** Phylogenetic analysis for SLC (B), NFL (C), BMP5-8 (D), and LOX (E) are shown as distance trees produced by Bayesian inference, with node probabilities shown, and candidates indicated in red. Species included are echinoderm: Lv, *Lytechinus variegatus*; Sp, *Strongylocentrotus purpuratus*; vertebrate: Hs, *Homo sapiens*; Mm, *Mus musculus*; Rn, *Rattus norvegicus*; Oc, *Oryctolagus cuniculus*; Gg, *Gallus gallus*; Xt, *Xenopus tropicalis*; Dr, *Danio rerio*; Bt, *Bos taurus*; Lc, *Latimeria chalumnae*; Tg, *Taeniopygia guttata*; invertebrate chordate: Ci, *Ciona intestinalis*; Cs, *Ciona savignyi*; and arthropod: Dm, *Drosophila melanogaster*.

Development • Supplementary information

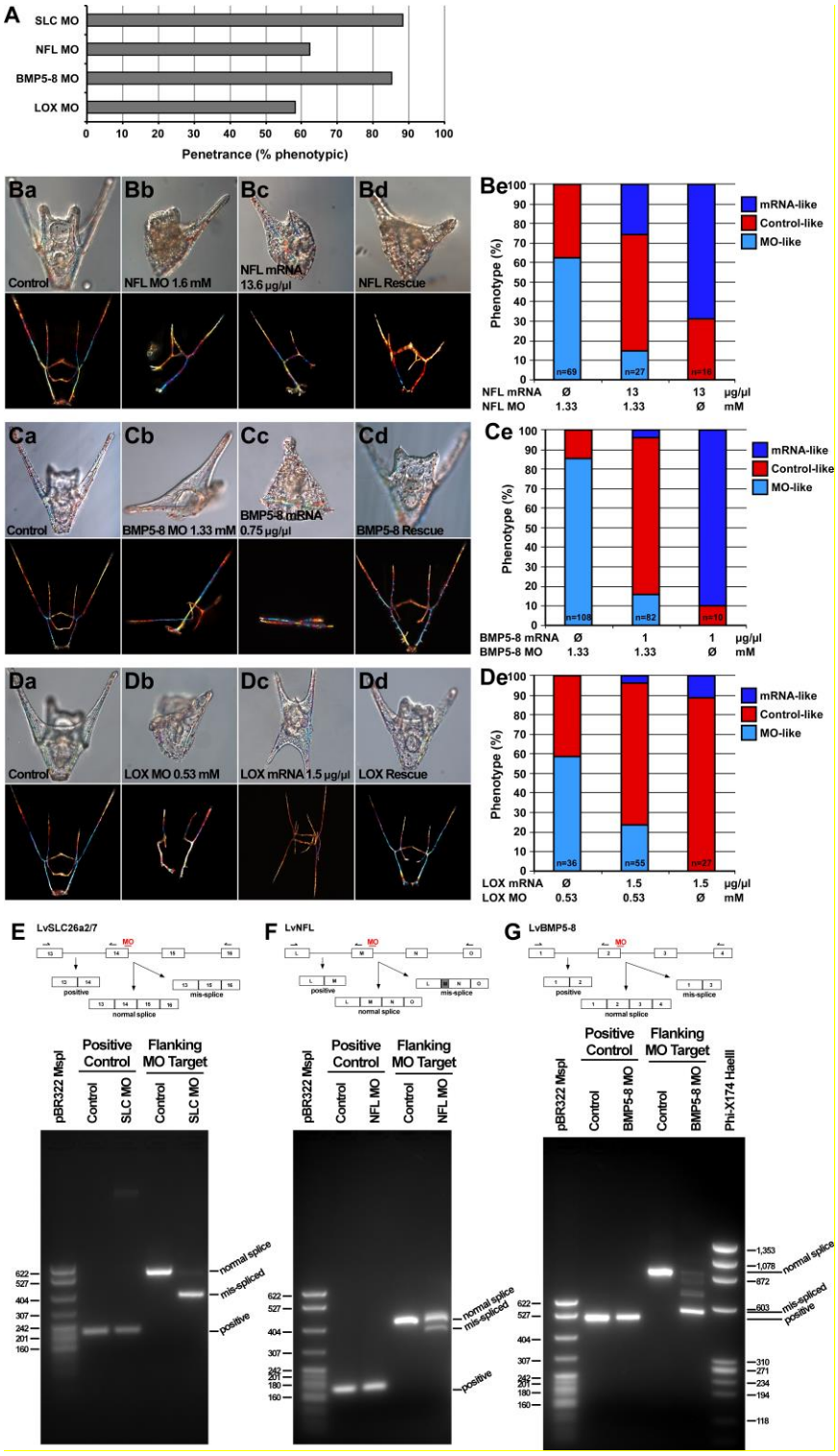

Figure S3. Skeletal patterning gene MOs are specific. A. Penetrance of SLC, NFL, BMP5-8 and LOX MOs as determined by percent of phenotypic embryos. **B-D.** Rescue experiments were performed for NFL (D), BMP5-8 (E), and LOX (F). Exemplar phenotypes are shown for control, LOF, GOF and rescued plutei by DIC (upper panels) and skeletal images (lower panels), and quantitated to determine reproducibility (De, Ee, Fe). MO and mRNA doses for rescued plutei are indicated in the graphs. See Figure 3T-3Y for SLC MO specificity controls. **E-G**. Splice analysis for control, SLC MO- (1.33 mM; E), NFL MO- (1 mM; F), and BMP5-8 MO-injected (2 mM; G) embryos at LG stage, showing an amplicon upstream the MO target site ("positive control") and another that spans the MO target site ("flanking MO target") as indicated in the schematics.

Development • Supplementary information

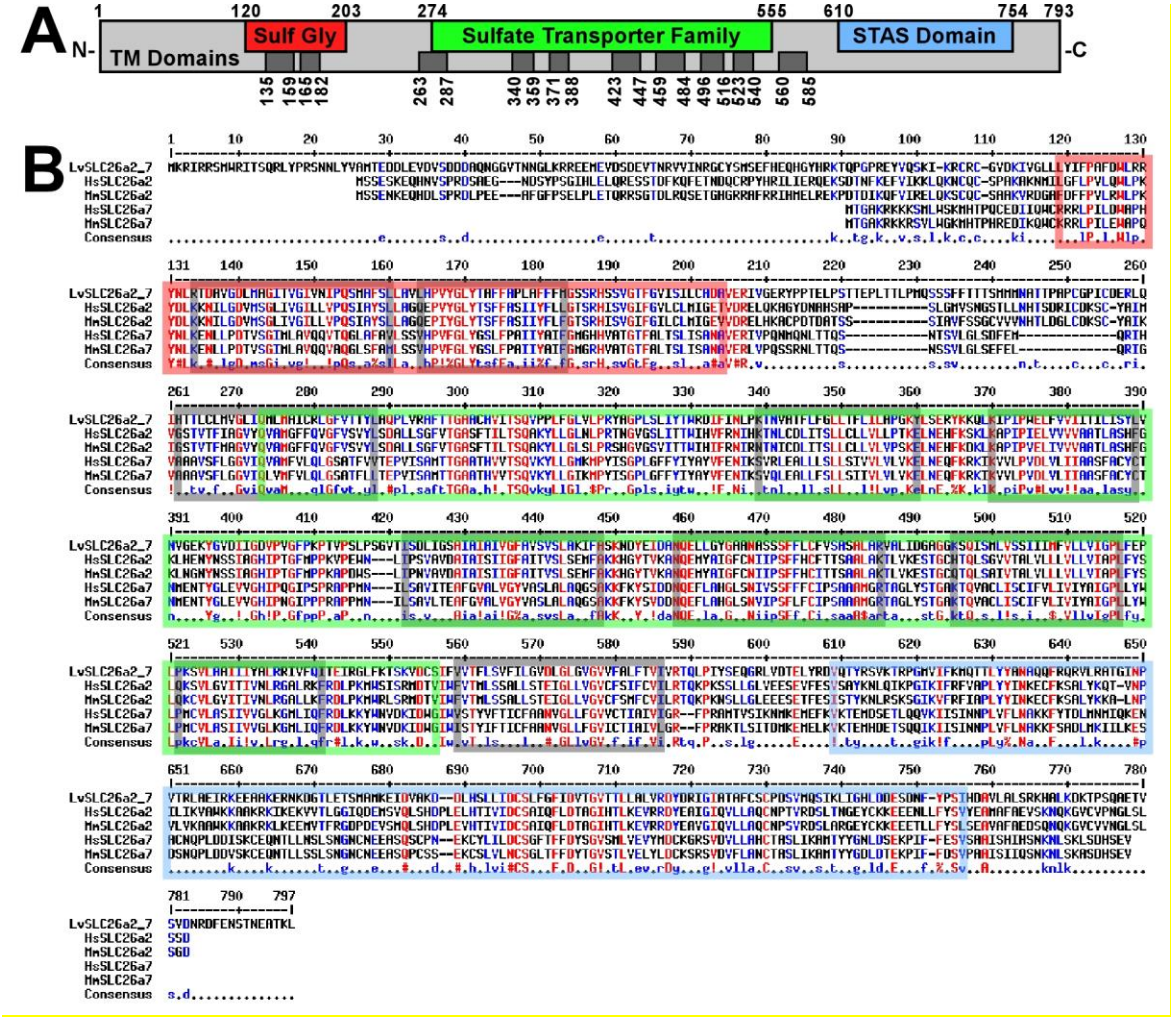

Figure S4. Sequence analysis indicates that LvSLC26a2/7 is most similar to vertebrate SLC26a2 and SLC26a7 genes. A. LvSLC26a2/7 conserved domains include Sulf Gly (sulfate transporter N-terminal domain with GLY motif, red), Sulfate Transporter Family (green), and STAS (sulfate transporter and anti-sigma factor antagonist, blue). Predicted transmembrane domains are indicated as dark grey boxes. Amino acid numbers above and below the schematic indicate domain boundaries. **B.** Predicted LvSLC26a2/7 amino acid sequence alignment with Hs and Mm SLC26a2 and SLC26a7 translations are displayed with conserved domains boxed, following the color scheme in A.

Development • Supplementary information

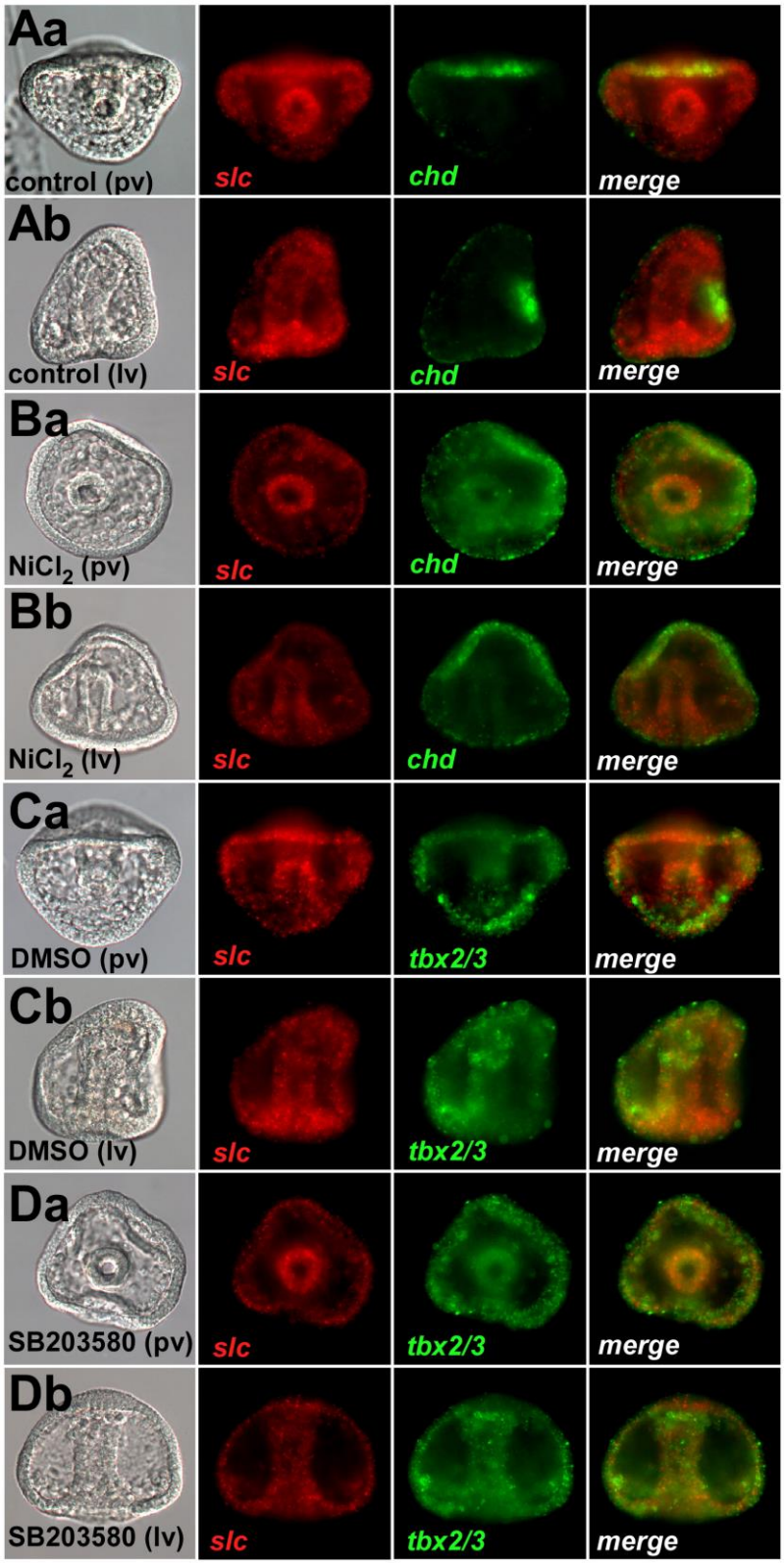

Figure S5. LvSLC26a2/7 expression is suppressed in sea urchin embryos treated with Ni or SB. Fluorescent *in situ* hybridization for *slc26a2/7* (*slc,* A-D, red) and either ventrally-expressed *chordin* (*chd*) (A-B, green), or dorsally-expressed *tbx2/3* (C-D, green) in untreated (A) or vehicle-treated (DMSO; C) controls, or in Ni- (B) or SB- (D) treated embryos at late gastrula stage, in posterior views (pv; Aa,Ba,Ca,Da) and lateral views (lv; Ab,Bb,Cb,Db).

Development • Supplementary information

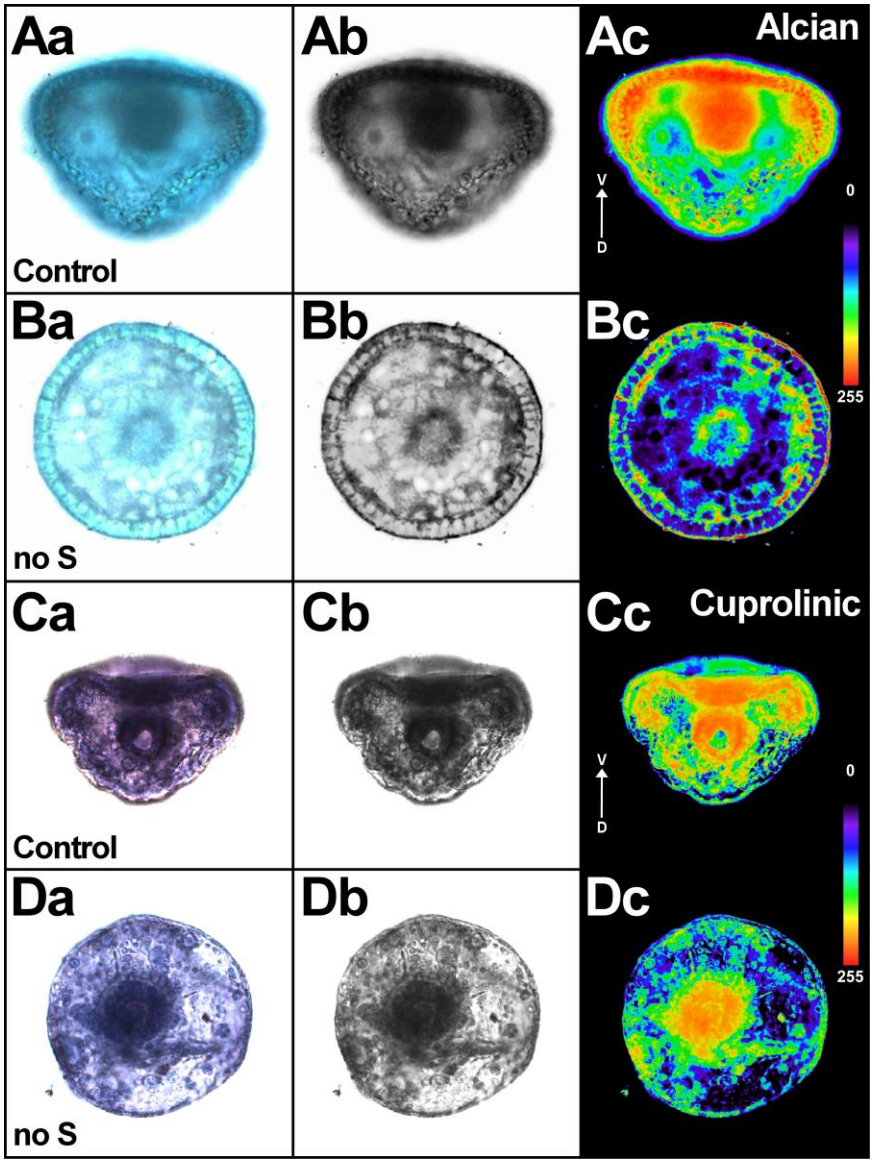

Figure S6. Alcian blue and Cuprolinic acid staining highlights ventral SPG accumulation in control embryos. Control embryo (A,C) and embryo cultured in sulfur free sea water (B,D) at LG stage were stained with Alcian blue (A,B) under SPG-specific conditions, or with Cuprolinic acid (C,D). Raw images (a) were converted to gray scale and subjected to histogram normalization (b), then a custom rainbow look up table (insets) was applied (c). The dorsal-ventral axis is indicated. Note that the fixation conditions for Cuprolinic acid results in shrinking of the embryo.

Development • Supplementary information

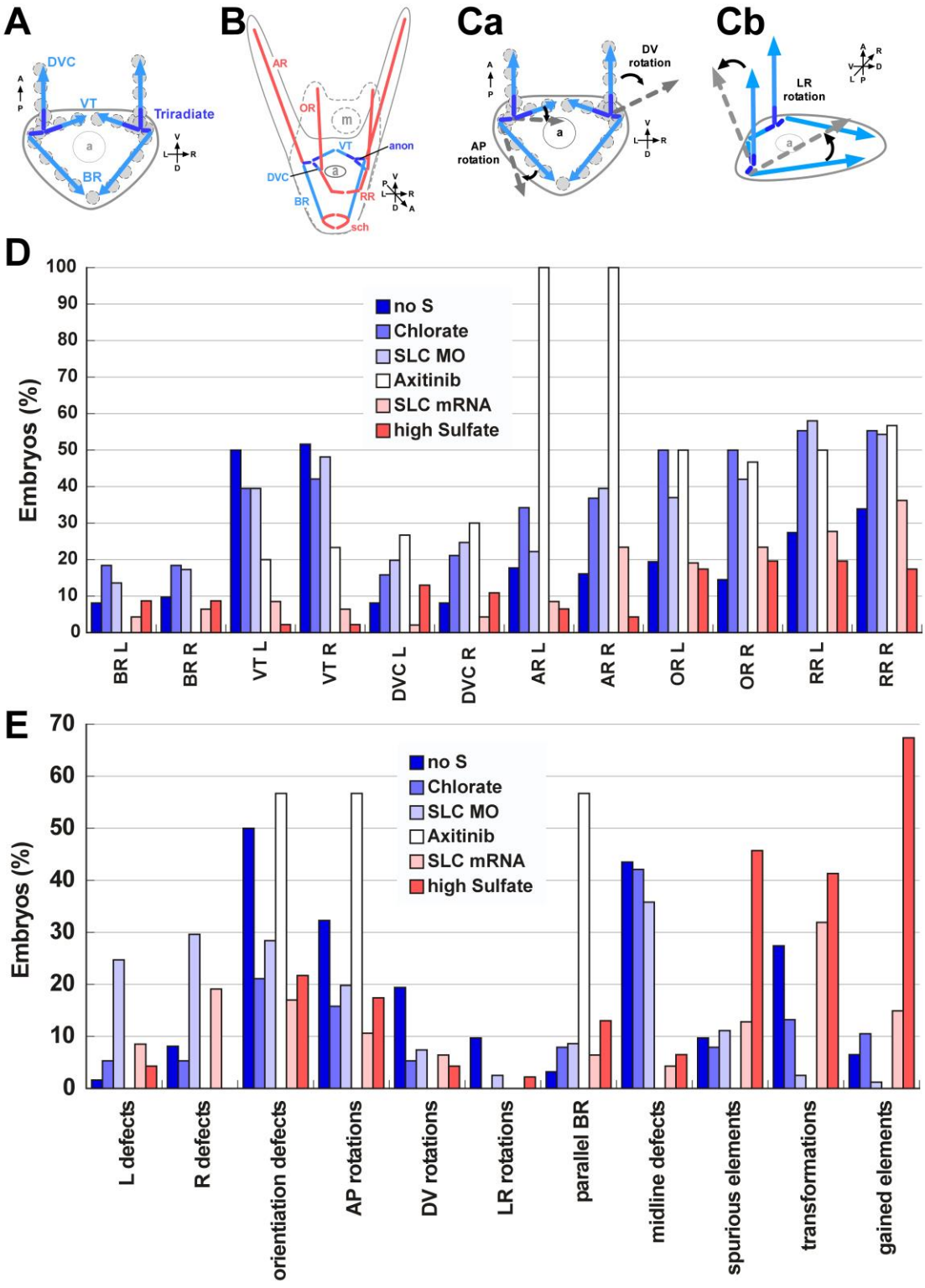

Figure S7. Skeletal scoring analysis highlights significant skeletal patterning defects in sea urchin embryos. **A.** Schematic displaying the primary skeleton at late gastrula stage. The initial triradiates (dark blue) in the ventrolateral PMC clusters extend into the ventral PMC ring to produce the ventral transverse rods (VTs), into the PMC cords to produce the dorsoventral connecting rods (DVCs), and laterally to produce the anonymous rods (anon), which extend only slightly before branching. The primary skeletal elements (light blue) also include the

Development • Supplementary information

body rods (BRs), which branch from the anonymous rods and extend into the dorsal PMC ring. The anus (a) is indicated. **B.** Schematic depicting the skeleton at pluteus stage. Here, the secondary skeleton is indicated in red, and includes the posterior anal rods (ARs), which branch ventrally from the anonymous rods, the posterior scheitel (sch), which branches from the dorsal tips of the body rods, and the anterior oral rods (ORs) and recurrent rods (RRs), which branch from the dorsoventral connecting rods (DVCs). Production of the secondary skeleton requires PMC migration out of the initial ring-and-cords pattern. The anus (a) and mouth (m) are indicated. **C.** We developed a skeletal patterning scoring rubric, which included scoring losses and gains for the elements shown in B, as well as a range of additional defects including left and right side-biased losses, midline defects, spurious elements, element transformations, and skeletal orientation defects. We classified orientation defects as rotations about the anterior-posterior (Ca), dorsal-ventral (Ca), or left-right (Cb) axis. Some embryos exhibited more than one orientation defect. Midline defects are defined as the absence of skeletal elements from the left-right midline of the pluteus (i.e., short or absent VTs and RRs, and absent sch). Spurious elements are defined as elements present where no element would normally develop, while gained element refers to duplications of normal rods. For rotational defects, embryos were counted if at least one element was appropriately perturbed, while LR defects were counted for an LR imbalance of at least two rods. In cases where the presence of an element was ambiguous because of the orientation of the embryo, we assumed the element was present. **D-E.** The frequency of skeletal patterning defects, with left (L) and right (R) side elements scored independently for pluteus stage larvae following SLC/SPG perturbation (no S, Chlorate, SLC MO, SLC mRNA, high Sulfate) or VEGF inhibition (Axitinib). Skeletal losses (D) and additional defects (E) are shown. Data are depicted as the percentage of embryos exhibiting each defect. Sample sizes are: no S, 62; chlorate, 38; SLC MO, 81; axitinib, 30; SLC mRNA, 47; high sulfate, 46. Fig. 3 and Fig. 5 depict selected portions of these results. Uninjected controls (n=34) and GST MO-injected controls (n=18) show normal skeletal development in 100% of the embryos, and are not graphically displayed.

Development • Supplementary information

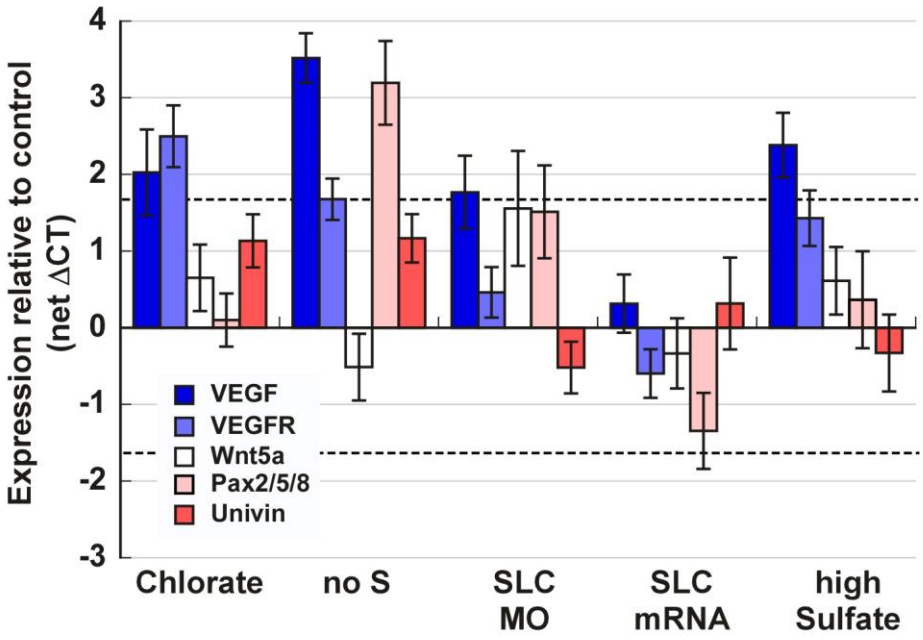

Figure S8. VEGF and/or VEGFR expression level is upregulated by SLC/SPG perturbations.
The expression of VEGF, VEGFR, Wnt5a, Pax2/5/8, and Univin relative to controls was determined by qPCR at late gastrula stage following SLC/SPG perturbations described in Figures 3 and 4. The results are displayed as normalized ΔC_T values ± s.e.m. Dashed lines indicate the threshold of significance at ΔC_T of 1.7 (approximately 3-fold).

Development • Supplementary information